Nucleation of creases and folds in hyperelastic solids is not a local bifurcation

Shrinidhi Pandurangi, Andrew Akerson, Ryan Elliott, Timothy Healey, Nicolas Triantafyllidis

Version of Record: https://www.sciencedirect.com/science/article/pii/S0022509621003537
Manuscript_cf9027bf6e091460fe479c403ea410d6

Nucleation of Creases and Folds in Hyperelastic Solids is Not a Local Bifurcation

Shrinidhi S. Pandurangi[a], Andrew Akerson[b], Ryan S. Elliott[b], Timothy J. Healey[c,a], Nicolas Triantafyllidis[d,e,f,*]

[a] *Field of Theoretical and Applied Mechanics, Cornell University, Ithaca, NY, USA*
[b] *Department of Aerospace Engineering and Mechanics, University of Minnesota, Minneapolis, MN 55455, USA*
[c] *Department of Mathematics, Cornell University, Ithaca, NY, USA*
[d] *LMS, École Polytechnique, CNRS UMR7649, Institut Polytechnique de Paris, 91128 Palaiseau, France*
[e] *Département de Mécanique, École Polytechnique, Palaiseau 91128, FRANCE*
[f] *Aerospace Engineering Department & Mechanical Engineering Department (emeritus) The University of Michigan, Ann Arbor, MI 48109-2140 USA*

Abstract

We consider creases and folds in compressed hyperelastic solids from the point of view of bifurcation theory. They refer to highly localized surface deformations that occur at compressive loads significantly below the value of the well-known Biot instability. Much work from the literature attempts to make the case that this phenomenon corresponds to a "*local bifurcation*" distinct from the Biot instability. A local bifurcation is a path of equilibrium solutions emanating from a (bifurcation) point on the trivial solution branch that exists in all sufficiently small neighborhoods of that bifurcation point. The inference is usually made by first introducing a small surface imperfection; a solution curve is then obtained that is seemingly close to a perfect bifurcation diagram. However, imperfection theory is valid only in some sufficiently small neighborhood of a bifurcation point. Thus, in the absence of an equilibrium path connecting these solutions to the trivial one, there is no justification for concluding that creasing and folding are *local bifurcations* of the perfect system.

In this work, we directly address the nucleation of these solutions in the perfect, imperfection-free case. We demonstrate that surface instabilities in functionally graded and bilayer elastic halfspaces, corresponding to local bifurcations from the homogeneous state, are necessarily smooth and oscillatory; creases/folds eventually do develop along the global bifurcating solution branches, albeit "*far*" from the trivial solution, as evidenced by the corresponding bifurcation diagrams. In addition, we find that their stable realization occurs at load levels well below that of the initial surface instability. Moreover, we obtain such results for the *perfect homogeneous halfspace*, by switching the continuation parameter from macroscopic lateral strain to the film-to-substrate shear modulus ratio. When this ratio reaches unity, we obtain the desired localized deformation solution, avoiding the need for analysis near the highly degenerate homogeneous state at the Biot instability.

Keywords: Energy methods, Nonlinear elasticity, Localization, Bifurcation, Symmetry

*Corresponding author.
Email address: nicolas.triantafyllidis@polytechnique.edu (Nicolas Triantafyllidis)

Contents

1. Introduction

The classic stability problem of the axially compressed nonlinear hyperelastic halfspace was first presented by Biot (1963). In his linearized analysis of the homogeneous, perfect halfspace's surface wrinkling, he established the critical strain for the onset of this phenomenon[1] with its arbitrary wavelength and eigenmode having an exponentially decaying amplitude away from the free surface. It was subsequently established that this phenomenon also occurs under tension on the surfaces of axially strained elastoplastic bars by Hill and Hutchinson (1975) as well as under finite strain bending by Triantafyllidis (1980). Similar phenomena were found to occur in the case of functionally graded materials (e.g. see Lee et al. (2008)) and in thin films on compliant substrates (e.g. see Audoly and Arezki (2008a)), where in contrast to the perfect, homogeneous halfspace, a finite wavelength for the eigenmode can be determined.

Of particular interest here is Biot's instability, the nucleation and subsequent evolution of a small-amplitude surface waviness to a highly localized deformation corresponding to folds or creases. Following the experiments of Gent and Cho (1999) and the influential investigations of Hohlfeld and Mahadevan (2011, 2012), new life has recently been injected into this problem due to the observation — at compressive loads significantly below the Biot instability — of highly localized deformation regions known as "*creases*" (i.e. crack-like regions of surface self-contact) and "*folds*" (i.e. regions of surface self-contact forming a void). In particular, Hohlfeld and Mahadevan (2011) study the bending (to break the challenging translational symmetry of the perfect Biot problem) of a finite strip and perform finite element simulations, regularized through the use of Hermite polynomial shape functions and the introduction of surface beam elements. They find creased configurations with a crease depth that approaches zero as the surface beam stiffness tends to zero. The resulting crease depth vs. compression plots show a "*T-shaped*" diagram which the authors term a "*nonlinear instability*" in Hohlfeld and Mahadevan (2011). In Hohlfeld and Mahadevan (2012), they perform a further analysis and present bifurcation diagrams indicating that the phenomenon is a "*local bifurcation*"[2] occurring for loads significantly below the Biot instability. These observations have led to an impressive amount of subsequent experimental and modeling work in the mathematical and engineering literature. In many cases these subsequent works claim the local bifurcation nature of the creasing/folding instabilities through the use of numerical imperfection methods. Additionally, and independently of the study of creases as an evolution to Biot's surface instability problem, self-folding surface deformation patterns have also been studied. First as part of universal solutions in incompressible, finite elasticity by Singh and Pipkin (1965) and subsequently in compressible, nonlinear elastic solids (e.g. see Silling (1991); Ciarletta (2018)).

A detailed review of the voluminous literature on this subject is beyond the scope of the present work; the interested reader is referred to the extensive review article by Li et al. (2012). However some references are given below in order to discuss the prevalent, imperfection-based approach in the literature for numerically calculating creases and folds, and to contrast this approach with our imperfection-free local bifurcation and global solution branch following methodology based on group-theoretic tools, which was introduced for this class of problems in Pandurangi et al. (2020).

In the recent mechanics literature pertaining to the development of folds, the work on "*ruga mechanics*" by Diab et al. (2013); Diab and Kim (2014); Zhao et al. (2015a, 2016) focuses on the development of folds and creases in functionally graded and bilayer configurations. These problems admit a finite wavelength for the Biot surface instability, which guides the selection of imperfections needed to find the creased and folded solutions by numerical methods (FEM) Chen et al. (2012, 2014); Jin et al. (2014, 2015). The transition from wrinkles – Biot surface instability – to creases was concurrently studied, for halfspaces as well as bilayers, by Cao and Hutchinson (2012); Hutchinson (2013), who showed, using Koiter's post-bifurcation asymptotic analysis, that the wrinkled paths are unstable and strongly imperfection sensitive. Akerson and Elliott (2021) have recently showed, using imperfection-free methods, that the stability of the initial post-bifurcation wrinkles depends strongly on the through-thickness spatial gradient of the shear modulus

[1] This is related to the "*complementing condition*" (see Agmon et al. (1964); Simpson and Spector (1987); Negrón-Marrero and Montes-Pizarro (2011)) used for boundary value problems with traction boundary conditions.

[2] A "*local bifurcation*" is a path of nontrivial solutions emanating from a (bifurcation) point on the trivial solution branch that exists in all sufficiently small neighborhoods of the bifurcation point.

μ (fiber-to-substrate stiffness ratio μ_f/μ_s for bi-layers or exponential rate constant for continuously graded systems).

Although the main thrust of research focuses on calculating folded and creased solutions in a two-dimensional (plane strain) context, efforts have also been directed at investigating the three-dimensional aspects of the problem using Von-Karman plate theory combined with a linear elastic halfspace Audoly and Arezki (2008a,b); Audoly and Azreki (2008) or fully nonlinear continua Zhao et al. (2015b); Chen et al. (2018). An additional reason for the revival of the Biot Problem is its importance in "*soft solids*" and biological problems, such as the problems of "*unfolding the sulcus*" Hohlfeld and Mahadevan (2011, 2012), "*elastosis in arteries*" Eskandari et al. (2016), and the instabilities associated with the clogging of arteries.

It is well-known that a linearized stability analysis of the flat surface of a halfspace predicts wrinkles (see Biot (1963)), indicating that a *local bifurcation* from a flat state to a creased/folded one is not possible. A straight-forward application of the implicit function theorem (see for example page 7 of Kielhöfer (2012), for the PDE version of this classic theorem) shows that *a local bifurcation is not possible, unless the linearized stability operator becomes singular*. For the problem at hand, it is well-known that this first occurs at the Biot load. Despite this, the methods employed in the existing literature — as in all of the above mentioned references (excluding Akerson and Elliott (2021)) — avoid this inconvenient fact by introducing an "*a priori*" imperfection biasing the system toward a desired configuration.[3] However, imperfection theory is only valid in all sufficiently small neighborhoods of a bifurcation point (e.g. Iooss and Joseph (1990)), i.e. there is no known "*global imperfect bifurcation theory*" (see Marsden and Hughes (1983)). Indeed, drawing mathematically precise conclusions from numerical global continuation in the presence of imperfections is risky, as pointed out in Healey (1989). It is exactly this issue which we aim to eliminate from the study of creases and folds with our present work. Accordingly, we employ the imperfection-free local bifurcation and global solution branch following method introduced by Pandurangi et al. (2020) for the study of a beam on a nonlinear elastic foundation.

Due to the high degree of symmetry present in perfect structures, such as the one considered here, it is common to have multiple paths emerging from the same bifurcation point. As a consequence, even near a bifurcation point the use of numerical "*imperfection methods*" for bifurcation problems is insufficient to thoroughly discover and organize the rich solution set. Accordingly, we employ a rigorous and systematic group-theoretic framework that enables the prediction of all generic bifurcations, each based on its geometric symmetry group. This approach draws on "*equivariant bifurcation theory*" (Golubitsky et al. (1988); Chossat and Lauterbach (2000); Ikeda and Murota (2010)) and is integrated with efficient numerical branch-following algorithms (Keller (1987); Healey (1988); Gatermann and Hohmann (1991); Wohlever and Healey (1995); Allgower and Georg (2003)) to create a robust, consistent methodology for the theoretical and numerical study of highly-symmetric (imperfection-free) bifurcation problems.

In this work we address the thus far poorly understood (see Yang et al. (2021)) issue of "*fold/crease nucleation*" in hyperelastic solids. We show that highly localized (creased) stable equilibrium solutions evolve "*far*" from the initial smooth and oscillatory bifurcation near the flat trivial solution, as evidenced by the corresponding bifurcation diagrams of amplitude ξ, energy change $(\mathcal{E}-\mathcal{E}^0)$ and axial force change $(\mathcal{E}-\mathcal{E}^0)_{,\varepsilon}$ versus the applied lateral macroscopic strain ε. Furthermore, we show that isolated stable creases (i.e., a single crease surrounded by long flat regions) evolve, along the *long wavelength secondary bifurcating paths*, far from the flat trivial solution. These secondary paths bifurcate in a cascading fashion from the short wavelength, wrinkled, primary bifurcation paths. These primary paths in turn emerge from the system's symmetry-breaking bifurcation points along its flat configuration path. Moreover, by switching control parameters in a bilayer problem using the film-to-substrate stiffness ratio, we obtain isolated crease solutions in the perfect homogeneous halfspace without ever using an imperfection.

We present the theoretical aspects of the boundary value problem in Section 2 and the numerical method in Section 3. The perfect bifurcation diagrams and stability results for the functionally graded and bilayer structures are given in Section 4. The constitutive law dependent evolution of the primary bifurcation orbits into creases and folds is studied. We also show how one can obtain isolated localized deformation

[3]The "*imperfection*" can be either of geometric nature – the more frequently used method – or in the form of a lateral force, as more recently proposed by Yang et al. (2021).

solutions in a perfect homogeneous halfspace without using an imperfection, and thus avoiding the need for analysis near the highly degenerate homogeneous state at the Biot instability. This is achieved by switching control parameters in the bilayer problem – using the ratio of film-to-substrate shear moduli instead of the lateral strain – and following the equilibrium path until the value of this ratio reaches unity. This same multiparameter approach has been employed in nearly singular problems for phase transitions with small interfacial energy in Healey and Miller (2007) and for wrinkling of highly stretched thin films in Healey et al. (2013). Conclusions are presented in Section 5. A brief presentation of relevant group theory and how it applies to the problem at hand is provided in Appendix A. Proof of local stability (polyconvexity) of the chosen material model, and expressions for stress and moduli tensors along the principal solution are given in Appendix B. Finally, the influence of mesh sensitivity on the bifurcated orbits – due to the presence of infinitely short wavelength instabilities at adequately large strains – is presented in Appendix C.

2. Theory

This section presents the theoretical aspects of the model. The boundary value problem is discussed in Subsection 2.1 and the stability of the problem's equilibrium solutions is presented in Subsection 2.2. The constitutive laws for the materials considered (representing rubber, polymeric foams and biological tissues) are discussed in Subsection 2.3. The symmetry group of the problem appears in Subsection 2.4 while its principal solution is presented in Subsection 2.5.

2.1. Boundary Value Problem

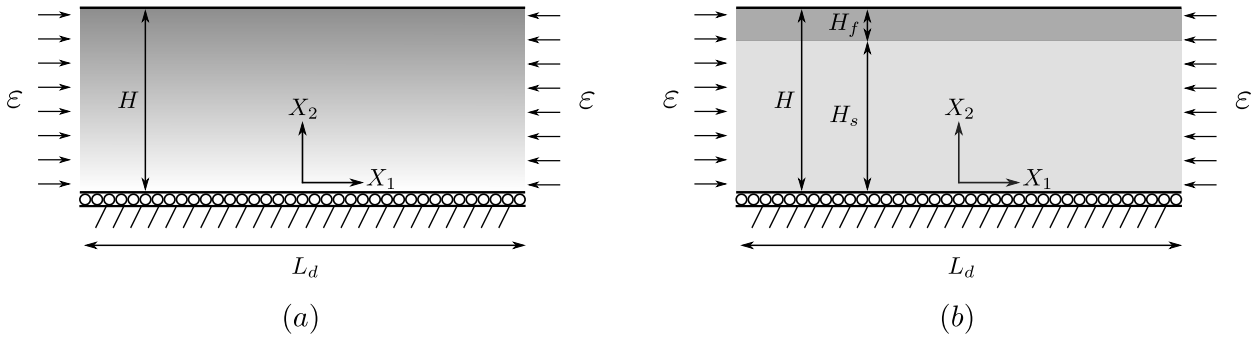

Figure 1: Schematics of the 2D layer model: (a) the functionally graded layer and (b) the film-substrate system.

Here, the general formulation of Akerson and Elliott (2021) is adopted and extended. The plane strain, 2D model adopted here is that of an infinite extent (along X_1) hyperelastic layer, with thickness H and X_2-dependent material properties, as seen in Figure 1.

Two cases are considered: a) the layer consists of a functionally graded material, i.e. its material properties are continuous functions of X_2 and b) the layer's material properties are piecewise constant along X_2, corresponding to a thin film of thickness H_f perfectly bonded to a much thicker substrate of thickness $H_s \gg H_f$. The layer thus occupies the domain $\Omega \equiv \{(X_1, X_2) : X_1 \in \mathbb{R},\ 0 \leq X_2 \leq H\} \subset \mathbb{R}^2$ in the reference configuration. The bottom surface of the layer $\partial\Omega_1 \equiv \{(X_1, X_2) : X_1 \in \mathbb{R},\ X_2 = 0\}$ is restricted to the $X_2 = 0$ line but allowed to freely slide along X_1 (i.e. shear-free), while its top surface $\partial\Omega_2 \equiv \{(X_1, X_2) : X_1 \in \mathbb{R},\ X_2 = H\}$ is traction-free.

A far-field compressive stretch of $0 < \lambda_1 \leq 1$ is applied to the layer along the X_1 direction, as seen in Figure 1. We define $\varepsilon \equiv 1 - \lambda_1$ to be the loading parameter of the layer. A Lagrangian formulation of the problem is adopted; a point at $\mathbf{X}$ in the undeformed (stress-free), reference configuration occupies position $\mathbf{x}$ in the deformed (stressed), current configuration. The layer consists of a hyperelastic material of energy density $W(\mathbf{F}; X_2)$ per unit reference area, where $\mathbf{F}$ is the local deformation gradient. In order to make the problem manageable – and deal with compact symmetry groups – we consider the L_d-periodic solutions,

defined on the finite subdomain[4] $\Omega_d \equiv \{(X_1, X_2) : -L_d/2 \le X_1 \le L_d/2,\ 0 \le X_2 \le H\} \subset \Omega$, and choose $L_d/H \gg 1$. The total potential energy (per unit reference length) of the system is hence given by[5]

$$
\begin{aligned}
&\mathcal{E}(\mathbf{u};\varepsilon) = \frac{1}{L_d}\int_{\Omega_d} W(\mathbf{F};X_2)dA\ ; \quad \mathbf{F} \equiv \nabla\mathbf{x}(\mathbf{X}) = \overset{0}{\mathbf{F}}(\varepsilon) + \nabla\mathbf{u}(\mathbf{X})\ ,\\
&\overset{0}{\mathbf{F}}(\varepsilon) = \mathrm{diag}[\lambda_i(\varepsilon)]\ , \quad \mathbf{x}(\mathbf{X};\varepsilon) = \overset{0}{\mathbf{F}}(\varepsilon)\cdot\mathbf{X} + \mathbf{u}(\mathbf{X};\varepsilon)\ ;\ \forall \mathbf{X} \in \Omega_d\ ,\\
&\int_{-L_d/2}^{L_d/2} u_1(X_1,0)dX_1 = 0\ , \quad u_2(X_1,0) = 0\ ;\ \forall X_1 \in [-\frac{L_d}{2},\frac{L_d}{2}]\ ,\\
&\mathbf{u}(-\frac{L_d}{2},X_2) = \mathbf{u}(\frac{L_d}{2},X_2)\ ;\ \forall X_2 \in [0,H]\ .
\end{aligned}
\tag{2.1}
$$

The deformation is described by a uniform biaxial strain – corresponding to the principal equilibrium path, constant deformation gradient $\overset{0}{\mathbf{F}}(\varepsilon)$ – plus an additional displacement field $\mathbf{u} \in U$, where U denotes the space of admissible perturbation displacement functions.[6] Some appropriate growth conditions on W as $\det\mathbf{F} \to 0$ and $\|\mathbf{F}\| \to \infty$ are also tacitly assumed as to ensure a realistic energy density $W(\mathbf{F};X_2)$.

Pointwise equilibrium equations and natural boundary conditions are obtained by setting to zero the first variation[7] of the total potential energy functional defined in (2.1)

$$
(\mathcal{E}_{,\mathbf{u}},\delta\mathbf{u}) = \frac{1}{L_d}\int_{\Omega_d} \frac{\partial W(\mathbf{F};X_2)}{\partial\mathbf{F}} : (\nabla\delta\mathbf{u})\ dA = 0\ ;\ \forall\delta\mathbf{u} \in U \implies
\begin{cases}
\nabla\cdot\mathbf{S} = \mathbf{0}\ ;\ \forall\mathbf{X}\in\Omega_d\ ,\ \mathbf{S} \equiv \dfrac{\partial W(\mathbf{F};X_2)}{\partial\mathbf{F}}\ ,\\[2ex]
S_{12} = 0\ ;\ \forall\mathbf{X}\in\partial\Omega_{d1}\ ,\ S_{i2} = 0\ ;\ \forall\mathbf{X}\in\partial\Omega_{d2}\ ,
\end{cases}
\tag{2.2}
$$

where $\mathbf{S}$ denotes the first Piola-Kirchhoff stress tensor. We seek the equilibrium solutions for the layer structure as a function of the load parameter (imposed lateral compressive strain) ε.

Of interest here is also the work-conjugate quantity of the load parameter ε, which is shown to be the total lateral force applied at any cross-section $X_1 = const.$ of the structure. From the energy and the kinematic definitions in (2.1), one can show using integration by parts[8] that $\mathcal{E}_{,\varepsilon}$ equals the axial (lateral) force of the structure, i.e. the layer thickness integral of first Piola-Kirchhoff stress S_{11}, which – due to the absence of shear stresses at the boundaries $\partial\Omega_{d1}$ and $\partial\Omega_{d2}$ – is independent of the X_1 coordinate

$$
\mathcal{E}_{,\varepsilon} = \frac{d}{d\varepsilon}\left\{\frac{1}{L_d}\int_{\Omega_d}[W(\overset{0}{\mathbf{F}}(\varepsilon)+\nabla\mathbf{u}(\mathbf{X}))]\ dA\right\} = -\int_0^H [S_{11}(X_1,X_2)]\ dX_2 = -\int_0^H [S_{11}(0,X_2)]\ dX_2\ . \tag{2.3}
$$

The nonlinear boundary value problem defined by (2.2) admits a large symmetry group resulting in a complex structure with an infinite number of equilibrium paths. Equilibrium paths related by symmetry can be grouped into "*orbits*." Accordingly, it is more appropriate, for the problem at hand, to discuss "*orbits of equilibrium solutions*" than it is to speak of a single solution. However, for convenience of exposition, the two terms are used interchangeably. From the "*principal solution*" $\overset{0}{\mathbf{u}}(\mathbf{X};\varepsilon) = \mathbf{0}$, corresponding to the constant deformation gradient $\overset{0}{\mathbf{F}}(\varepsilon)$ (but no additional displacement, see (2.1)), an infinity of "*primary bifurcated*

[4] Analogous definitions hold for the corresponding bottom $\partial\Omega_{d1}$ and top $\partial\Omega_{d2}$ surfaces of the finite domain Ω_d.

[5] The X_2-dependent isotropic material properties adopted here give a homogeneous strain principal solution with transverse principal stretch ratio $\lambda_2(\varepsilon)$. For more general orthotropic, graded materials with arbitrary X_2-dependent properties, $\lambda_2(X_2;\varepsilon)$.

[6] The space U of admissible fields $\mathbf{u}$ consists of all continuous vector fields $\mathbf{u}(\mathbf{X})$ satisfying the zero vertical displacement at the bottom of the layer and periodicity boundary conditions in (2.1). Additionally, the integral constraint on u_1 excludes rigid body motion along the X_1 direction.

[7] By $(\mathcal{E}_{,\mathbf{u}},\delta\mathbf{u})$ we denote the scalar result of linear operator $\mathcal{E}_{,\mathbf{u}}$ – first functional derivative of $\mathcal{E}$ with respect to $\mathbf{u}$ – operating on an arbitrary admissible (test) function $\delta\mathbf{u} \in U$.

[8] Using the principle of virtual work where the kinematically admissible displacement field is the actual principal solution.

paths" (more precisely continuous orbits) emerge. From each one of these, "*secondary bifurcated paths*" with different periods also emerge. Additionally, "*tertiary bifurcated paths*" emerge from the secondary ones and so on. Although the symmetry group of each orbit is reduced at each bifurcation, enough symmetries remain to allow further bifurcations. The goal is to follow each one of these orbits, away from the bifurcation point of their origin and study their stability. The numerical solution of the boundary value problem given by (2.2) is presented in Section 4.

2.2. Stability of Equilibria

The problem at hand is conservative, with energy given by (2.1). To determine the stability of any equilibrium solution $\overset{0}{\mathbf{F}}(\varepsilon)\cdot\mathbf{X}+\mathbf{u}(\mathbf{X};\varepsilon)$ of (2.2), one may apply the *principle of minimum potential energy* and check if it is a local energy minimizer, i.e. check the positive definiteness of the self-adjoint bilinear operator $\mathcal{E}_{,\mathbf{uu}}$, evaluated at the investigated solution[9], by finding its eigenvalues β

$$((\mathcal{E}_{,\mathbf{uu}},\Delta\mathbf{u}),\delta\mathbf{u})=\beta\langle\Delta\mathbf{u},\delta\mathbf{u}\rangle\ ;\ \forall\delta\mathbf{u}\in U\ ,\quad \mathcal{E}_{,\mathbf{uu}}\equiv\mathcal{E}_{,\mathbf{uu}}(\overset{0}{\mathbf{F}}(\varepsilon)\cdot\mathbf{X}+\mathbf{u}(\mathbf{X};\varepsilon);\varepsilon)\ , \tag{2.4}$$

where $\Delta\mathbf{u}$ is the corresponding eigenmode and $\langle\cdot\ ,\ \cdot\rangle$ denotes an inner product in U. A stable solution corresponds to a positive minimum eigenvalue[10] β. For the stability of periodic solutions of period L (where $L<L_d$) one can take advantage of the Bloch-wave representation theorem, according to which any eigenmode $\Delta\mathbf{u}$ of the stability operator $\mathcal{E}_{,\mathbf{uu}}$ in (2.4) admits the following representation

$$\Delta\mathbf{u}(\mathbf{X})=\exp(i2\pi kX_1/L)\ \mathbf{p}(\mathbf{X})\ , \tag{2.5}$$

where $i=\sqrt{-1}$ is the imaginary unit, $\mathbf{p}(\mathbf{X})$ is L-periodic in the X_1 direction and[11] $k\in[0,1)$ is the wavenumber. Thus, the Bloch-wave representation reduces the eigenvalue problem (2.4) to a set of smaller dimensional ones (one such problem for each value of the wavenumber). By scanning all admissible values of k, one can find $\beta_{min}(k)$ for each fixed value of k.

For a well-posed problem, the neighborhood of the stress-free (unloaded) configuration near $\varepsilon=0$ is stable, i.e. $\beta_{min}(k;\varepsilon)\geq 0\ ;\forall k\in[0,1),\ 0\leq\varepsilon\ll 1$. As the applied compressive strain ε increases, stability of the uniform strain (principal) solution will be lost at the first bifurcation point encountered along the principal loading path at some ε_c, as elaborated in Subsection 4.1. The emerging primary bifurcation orbit will be found and followed until secondary bifurcations appear and so on.

2.3. Material Selection

We consider two types of material models: a weakly compressible *Neo-Hookean* material model, representative of a natural rubber, and a *power-law* material model that can be adjusted to represent open cell foams and soft biological tissues. For the Neo-Hookean material model we investigate two different layered structures: (a) functionally graded and (b) thin film, using an X_2-dependent shear modulus. Accordingly, for (a) we choose an exponentially varying shear modulus while for (b) a piecewise constant. For the power-law model we only consider the thin film case (b).

1. <u>*Neo-Hookean material model*</u> The stored energy density of the Neo-Hookean layer structure has an energy density[12]

$$W(\mathbf{F};X_2)=\mu(X_2)\left[\frac{1}{2}(I_1-2-\ln I_2)+\frac{\nu}{1-\nu}(\sqrt{I_2}-1)^2\right]\ , \tag{2.6}$$

[9] By $((\mathcal{E}_{,\mathbf{uu}},\Delta\mathbf{u}),\delta\mathbf{u})$ we denote the scalar result of the self-adjoint bilinear operator $\mathcal{E}_{,\mathbf{uu}}$ – second functional derivative of $\mathcal{E}$ with respect to $\mathbf{u}$ – operating on admissible functions $\Delta\mathbf{u},\ \delta\mathbf{u}\in U$.

[10] We find here continuous orbits of equilibria, symmetry-related but with the same energy, implying the existence of a zero eigenvalue of the stability operator $\mathcal{E}_{,\mathbf{uu}}$ in (2.4). Thus, all equilibria are, at best, neutrally stable. Accordingly, we ignore the zero eigenvalue associated with an equilibrium orbit and require that *all other* eigenvalues be positive for stability.

[11] Without loss of generality, we consider $L_d=qL,\ q\in\mathbb{N}$. From translational symmetry in (2.5) $k\in\mathbb{Q}$, i.e. $k=r/q;\ r,q\in\mathbb{N}, 1\leq r\leq q$. For $L_d\longrightarrow\infty$, i.e. for the stability of the infinitely long layer, we can consider $k\in\mathbb{R};\ 0\leq k\leq 1$.

[12] The logarithmic term $(\ln I_2)$ in the energy density drives it to infinity when the material's area is reduced to zero.

where ν denotes the (2D) Poisson's ratio in plane strain[13] (where $0 \leq \nu \leq 1$), μ denotes the shear modulus and I_1 and I_2 are the invariants of the right Cauchy–Green tensor $\mathbf{C} = \mathbf{F}^{\mathbf{T}} \cdot \mathbf{F}$ given by $I_1 = \mathrm{Tr}(\mathbf{C})$ and $I_2 = \det(\mathbf{C})$. Depending on the case (functionally graded layer or a film on a substrate), the shear modulus is

$$\mu(X_2) = \begin{cases} \mu(X_2) = \mu_0 e^{\alpha X_2} \; ; X_2 \in [0, H] \; , \quad \alpha > 0 & \text{for case (a)} \; , \\ \\ \mu(X_2) = \mu_s \; ; X_2 \in [0, H_s) \; , \quad \mu(X_2) = \mu_f \; ; X_2 \in [H_s, H] & \text{for case (b)} \; . \end{cases} \tag{2.7}$$

2. *power-law model* The power-law model has an adjustable power exponent p; it can thus model a *strain softening* material ($p < 1$, typical of open cell foams) or a *strain hardening* material ($p > 1$, typical of biological tissue)[14]. Since for $p \neq 1$ this model has undesirable properties (infinite stiffness for $p < 1$ and zero stiffness for $p > 1$) in its undeformed state $\mathbf{F} = \mathbf{I}$, a Neo-Hookean response is assumed ($p = 1$) in the neighborhood of small strains, i.e. for an equivalent shear strain $0 \leq \gamma \leq \gamma_y \ll 1$. A continuous stress state is ensured at transition, i.e. when the equivalent shear strain $\gamma = \gamma_y$. The corresponding energy density is

$$W(\mathbf{F}; X_2) = \mu(X_2) \left[\frac{c}{2} (I_1 - 2 - \ln I_2)^p + \frac{\nu}{1-\nu} (\sqrt{I_2} - 1)^2 \right] \; ,$$

$$\gamma \equiv (I_1 - 2 - \ln I_2)^{1/2} \; ; \quad \begin{cases} p = 1 \; , \quad c = 1 & \text{for } 0 \leq \gamma \leq \gamma_{\mathrm{y}} \; , \\ \\ p \neq 1 \; , \quad c = \dfrac{1}{p} (\gamma_y)^{2(1-p)} & \text{for } \gamma > \gamma_{\mathrm{y}} \; . \end{cases} \tag{2.8}$$

For the power-law material only the thin film structure is considered and $\mu(X_2)$ is given by case (b) in (2.7).

An important property of the selected constitutive law in (2.8) (of which the Neo-Hookean material is a special case at $p = 1$) is its "*local stability*," i.e. "*rank one convexity*." It is shown in Appendix B.1 that the stronger condition of *polyconvexity* applies for $p > 0.5$ and $\nu > 0.05$, thus guaranteeing rank one convexity for the values of p used in this work.

2.4. Symmetry

The symmetry group and the lattice of isotropy subgroups of this problem explaining the structure of the bifurcated equilibrium paths are well known, e.g. see Ikeda and Murota (2010). However, for reasons of clarity and completeness, we give here a brief presentation of the pertaining theory (Healey, 1988; Gatermann and Hohmann, 1991; Golubitsky et al., 1988; Chossat and Lauterbach, 2000; Field, 1996; Vanderbauwhede, 1982; Sattinger, 1979; Ikeda and Murota, 2010). For the layer model at hand, there exists a group G of transformations that leave its energy $\mathcal{E}(\mathbf{u}; \varepsilon)$ – defined in (2.1) – invariant under the action of all transformations $g \in G$. For practical purposes, we want to deal with a compact symmetry group G. To this end a maximum period L_d of all sought equilibrium solutions must be selected. In principle, the choice of L_d is limited only by the available computational resources. It is also desirable to choose L_d so that it is commensurate with (i.e., an integer multiple of) the fundamental period L_c of the primary bifurcation orbit[15]: $L_d = L_c q$ and $q \in \mathbb{N}$. Finally, it is important to point out that the selection of $q > 1$ facilitates the inclusion of "period-extending" (period-doubling, -tripling, etc.) solutions.[16]

The symmetry group G of the L_d-periodic, layered system with energy density given by (2.1), is the infinite, compact group $G = C_{\infty v} \simeq O(2)$. The generators of this group are denoted by $\{\sigma_v, c(\theta)\}$, where σ_v is the reflection about the plane $X_1 = 0$ and $c(\theta)$ is the phase shift by an angle $\theta \in [-\pi, \pi)$. The faithful representation of G on the space of admissible displacement functions $\mathbf{u}(\mathbf{X}) \in U$ are as follows

[13] The 2D Poisson ratio must satisfy $-1/2 < \nu < 1$ for plane strain linear elasticity, with incompressibility corresponding to $\nu = 1$; however the positivity of bulk energy in (2.6) dictates positive ν values.

[14] The terminology strain hardening ($p > 1$) or strain softening ($p < 1$) is due to the incompressible version ($\nu = 1$) of (2.8), where the shear modulus $\mu(\gamma) = 2p(2p-1)\gamma^{2(p-1)}$ is respectively an increasing or decreasing function of the shear strain γ.

[15] In Subsection 4.2 it is shown how one can determine L_c for the layer structure.

[16] Indeed, with (as below) $q = 4$, the primary bifurcation branch will have period L_c. Then each secondary bifurcating branch may be associated with one of the periods $L_r = rL_c$ with r divisor of q.

- Reflection σ_v with respect to the X_2 axis:

$$T_{\sigma_v}:\ U\longrightarrow U\ ,\quad T_{\sigma_v}\begin{bmatrix}u_1(X_1,X_2)\\ u_2(X_1,X_2)\end{bmatrix}=\begin{bmatrix}-u_1(-X_1,X_2)\\ u_2(-X_1,X_2)\end{bmatrix}\ . \tag{2.9}$$

- Phase-shift $c(\theta)$ by a phase angle $\theta\in[-\pi,\pi)$:

$$T_{c(\theta)}:\ U\longrightarrow U\ ,\quad T_{c(\theta)}\begin{bmatrix}u_1(X_1,X_2)\\ u_2(X_1,X_2)\end{bmatrix}=\begin{bmatrix}u_1\left(X_1+\dfrac{L_d\theta}{2\pi},X_2\right)\\ u_2\left(X_1+\dfrac{L_d\theta}{2\pi},X_2\right)\end{bmatrix}\ . \tag{2.10}$$

One can easily verify that energy density given by (2.1) is invariant under any transformation of $G=C_{\infty v}$

$$\mathcal{E}(T_g\mathbf{u};\varepsilon)=\mathcal{E}(\mathbf{u};\varepsilon)\ ;\quad \forall\mathbf{u}\in U\ ,\quad \forall\varepsilon\in[0,1)\ ,\quad \forall g\in C_{\infty v}\ . \tag{2.11}$$

The *fixed-point space* $\mathcal{S}_{C_{\infty v}}\equiv\{\mathbf{u}\in U: T_g\mathbf{u}=\mathbf{u}\ ,\ \forall g\in C_{\infty v}\}$ consists of fields $\mathbf{u}\in U$ that remain unaltered under the action of the group. It can be shown that these fields are of the form $u_1=0, u_2=f(X_2)$, where f is an admissible, arbitrary, real-valued function. The principal solution – also termed *fundamental solution* – is $\overset{0}{\mathbf{u}}(\mathbf{X};\varepsilon)=\mathbf{0}\in\mathcal{S}_{C_{\infty v}}$.

Attention is now turned to the action of symmetry group $C_{\infty v}$ on the bifurcated solutions. It will be shown in Section 4 that the primary bifurcation orbits have symmetry group C_{qv}, which is generated by $T_{\sigma_v}, T_{c_{(2\pi/q)}}$. These orbits can be calculated in the corresponding fixed point space $\mathcal{S}_{C_{qv}}$. It will also be shown that secondary bifurcation orbits emerge from the primary one, each with a (lower) symmetry group C_{rv}, generated by $T_{\sigma_v}, T_{c_{(2\pi/r)}}$, where $r\in\mathbb{N}$ with $1\le r\le(q-1)/2$ or $1\le r\le q/2$ for an odd or even q, respectively. These orbits can be calculated in the corresponding fixed point space $\mathcal{S}_{C_{rv}}$. All of these bifurcations, i.e. from fundamental to primary orbit and from primary to secondary orbits are found to be *pitchfork bifurcations* (i.e. symmetric). The reader is referred to Appendix A for details.

2.5. Principal Solution

The principal solution of the problem $\overset{0}{\mathbf{u}}(\mathbf{X};\varepsilon)=\mathbf{0}$ is the solution of (2.2) corresponding to a constant strain field $\overset{0}{\mathbf{F}}(\varepsilon)=\mathrm{diag}[\lambda_1(\varepsilon),\lambda_2(\varepsilon)]$, due to the adopted form of the constitutive law in (2.7) and (2.8) where only the shear modulus $\mu(X_2)$ is spatially-dependent but the Poisson ratio ν is constant. The transverse principal stretch ratio $\lambda_2(\varepsilon)$ is found in terms of the axial stretch ratio $\lambda_1(\varepsilon)=1-\varepsilon$ from the requirement that the transverse normal stress vanishes ($S_{22}=0$), as dictated by equilibrium and the free surface $\partial\Omega_{d2}$ boundary condition in (2.2), giving the following relation between the principal stretches

$$pc[\lambda_1^2+\lambda_2^2-2-2\ln(\lambda_1\lambda_2)]^{p-1}\left(\lambda_2^2-1\right)+\frac{2\nu}{1-\nu}\left(\lambda_1^2\lambda_2^2-\lambda_1\lambda_2\right)=0\ ;\quad \lambda_1=1-\varepsilon\ ,\ \lambda_2(\varepsilon)\ . \tag{2.12}$$

For a fixed $\lambda_1=1-\varepsilon\ ;\ \varepsilon\in[0,1)$, one can show that there will always exist at least one positive root λ_2 of (2.12), found numerically using the bisection method, as the closest to unity root of the above equation.

The resulting dimensionless axial compressive stress $|S_{11}|/\mu$ vs. strain ε response for the Neo-Hookean ($p=1$) and power-law models (strain hardening: $p>1$, and strain softening: $0.5<p<1$) for the principal solution are plotted in Figure 2. As discussed in (2.8), to avoid the singularity in the power-law stress-strain response at $\varepsilon=0$, is it assumed that $p=1$ in a neighborhood[17] $0\le\varepsilon\le\varepsilon_y$, where we chose $\varepsilon_y=0.05$.

[17] According to (2.8), ε_y is related to γ_y by $(\gamma_y)^2=(\lambda_1(\varepsilon_y))^2+(\lambda_2(\varepsilon_y))^2-2-2\ln[\lambda_1(\varepsilon_y)\lambda_2(\varepsilon_y)]$.

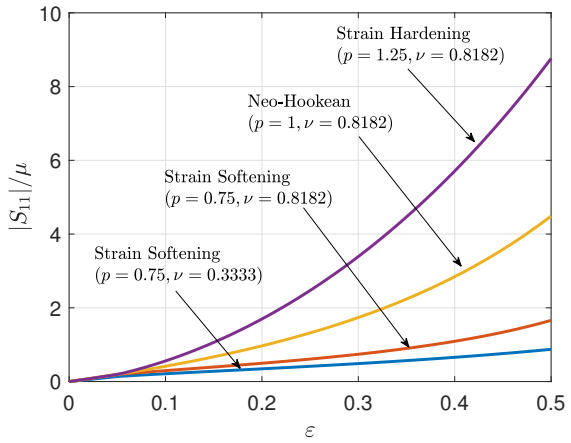

Figure 2: Dimensionless axial compressive stress component (1st Piola-Kirchhoff) $|S_{11}|/\mu$ vs. its work-conjugate strain ε for the Neo-Hookean and power-law constitutive laws used in the different layer models.

We recall here that the power-law models with $p = 0.75 < 1$ and $p = 1.25 > 1$ are selected to represent open cell foams and biological tissue, respectively, while the Neo-Hookean case $p = 1$ – used here for purposes of comparison with Akerson and Elliott (2021) – is a popular choice for polymeric materials. It is worth noticing in Figure 2 that for a constant power-law exponent p the reduction of the Poisson ratio ν results in a softer response, thus explaining the use in all subsequent calculations of the combination $p = 0.75,\ \nu = 0.3333$ for the softening and $p = 1.25,\ \nu = 0.8182$ for the hardening materials respectively.

3. Numerical Method

As discussed in Section 2, calculations are performed on a finite domain $\Omega_d = [-L_d/2,\ L_d/2] \times [0,\ H]$ with periodicity conditions on $\mathbf{u}$ applied at $X_1 = \pm L_d/2$, as dictated by (2.1). The domain Ω_d is discretized using a rectangular mesh with four node isoparametric quadrilaterals and a 2×2 Gauss integration scheme. The mesh is progressively refined from $X_2 = 0$ to the free surface $X_2 = H$ in order to capture the expected highly localized surface deformations. As a result of this discretization, a node with position vector $\mathbf{X}_n$ carries two degrees of freedom $u_1(\mathbf{X}_n)$, and $u_2(\mathbf{X}_n)$. We thus obtain from (2.1) the discretized energy $\mathcal{E}(\mathbf{v};\varepsilon)$ as a function of the discretized global displacement vector $\mathbf{v}$. A typical unit cell ($q = 1$, $L_d = L_c$) has 550 elements. For the largest domain discretized[18] ($q = 4$, $L_d = 4L_c$) we have $2,200$ elements. All the simulation codes are written using *deal.ii* (Alzetta et al. (2018)), a C++ finite element library.

From the group-theoretic considerations in Subsection 2.4 – recalling that $q = 4$ – the solutions on the primary and the secondary bifurcation orbits have C_{rv} symmetry where $r = 1, 2, 4$. Calculations are performed in the corresponding fixed point spaces $S_{C_{rv}}$, respectively on domains $\Omega_d^\star = [0, rL_c/2] \times [0, H]$, where the following kinematic boundary conditions, dictated by the invariance of the solution to transformations $T_{\sigma_v}, T_{c_{(2\pi/r)}}$ are used

$$u_1(0, X_2) = 0\ , \quad u_1(rL_c/2, X_2) = 0\ . \tag{3.1}$$

Due to the symmetry restrictions (3.1), we anticipate that the deformed configuration evolves into a highly localized surface region at $X_1 = 0$ on at least some of the bifurcated equilibrium paths. To avoid interpenetration of the material points, we include a repulsive self-contact force[19] through an in-plane

[18] Additional calculations with a more refined mesh of $8,800$ elements for the largest domain were also performed, but resulted in no appreciable change in the calculated orbits. See also Appendix C.

[19] Here we are interested in exploring the onset of evolution of bifurcated equilibrium paths up to the initiation of self contact. Thus, we use a simple discrete numerical penalty model for this purpose. Of course, to study the fine details of fully evolved creased and/or folded equilibrium configurations, a more sophisticated contact model, such as those used by Diab et al. (2013) and co-workers, must be used.

potential at the free surface in the finite element model. The implementation of this penalty-type method is described as follows. From the displacement degrees of freedom, we identify $u_1^{s_i}$ the components of the displacement in the X_1-direction of the 'i'th surface node. From (2.1), the X_1 component of position of the 'i'th surface node in the deformed configuration $\mathbf{x}^{s_i}$ is then given by

$$0 \le x_1^{s_i} = u_1^{s_i} + X_1^{s_i}\lambda_1(\varepsilon) \; . \tag{3.2}$$

Denote by $\mathbf{v}^s$ the vector of all[20] surface degrees of freedom u_1^s in Ω_d^*. To avoid interpenetration – which from symmetry with respect to the $X_1 = 0$ would imply $x_1^{s_i} < 0$ – we define a self-contact penalty energy $\mathcal{E}_{sc}$ as

$$\mathcal{E}_{sc}(\mathbf{v}^s;\varepsilon) = \sum_{i=1}^{\mathcal{S}} \frac{1}{2}\frac{\kappa}{(x_1^{s_i})^2} \; , \tag{3.3}$$

where $\mathcal{S} \in \mathbb{N}$ is the total number of surface nodes and $\kappa \ll 1$ is the penalty constant; a typical value of $\kappa = 10^{-12}$ is used in the calculations. Note that $\mathcal{E}_{sc}$ increases rapidly and blows up as a surface node approaches the $X_1 = 0$ axis, i.e. as $x_1^{s_i} \to 0^+$. The discretized total energy $\mathcal{E}_{tot}(\mathbf{v};\varepsilon)$ of the system is thus the sum of the discretized version of the energy in (2.1) plus the penalty term $\mathcal{E}_{sc}(\mathbf{v}^s;\varepsilon)$,

$$\mathcal{E}_{tot}(\mathbf{v};\varepsilon) = \mathcal{E}(\mathbf{v};\varepsilon) + \mathcal{E}_{sc}(\mathbf{v}^s;\varepsilon) \; . \tag{3.4}$$

The discrete set of nonlinear equilibrium equations $\partial\mathcal{E}_{tot}(\mathbf{v};\varepsilon)/\partial\mathbf{v} = \mathbf{0}$ are solved using a standard incremental Newton–Raphson method combined with pseudo arc-length continuation (see Keller (1987); Allgower and Georg (2003)), where the control parameter is the applied strain ε. Adaptive step-sizes are implemented to handle convergence during self-contact of surface nodes.

The stability of each equilibrium orbit is evaluated according to the Bloch wave method described in Subsection 2.2. Unlike the equilibrium path calculations that are performed in the half-domains Ω_d^*, the stability calculations are based on the full domain[21] Ω_d using the coupling condition in (2.5) for the $X_1 = \pm L_d/2$ boundary degrees of freedom,

$$\mathbf{v}(L_d/2, X_2) = \exp(i2\pi k)\mathbf{v}(-L_d/2, X_2) \; ; \quad k \in [0,1) \; . \tag{3.5}$$

In practice, to avoid using complex numbers in the numerical calculations, we use the method proposed by Aberg and Gudmundson (1997) that separates out real and complex parts. The method leads to the simultaneous solution of two systems of equations, one for real and another for complex parts, with a real stiffness matrix of almost twice the size of the unconstrained stiffness matrix resulting by the FEM discretization of $\mathcal{E}_{,\mathbf{uu}}$. An equilibrium solution is stable if its minimum eigenvalue is $\beta_{min} \ge 0$. Note that the translational mode is included in $k = 0$, giving always a zero eigenvalue (see discussion in Subsection 4.2 preceding (4.5)).

4. Results

This section presents the primary and secondary bifurcation equilibrium orbits and discusses their stability for the graded and layered models considered, all with a reference configuration thickness $H = 1.0$. For the functionally graded layer $\mu(0) = \mu = 1$ while for all bilayers $\mu_s = \mu = 1$. Consequently the energy reported in all subsequent calculations is the dimensionless energy $\mathcal{E}/H\mu$, with $\mathcal{E}$ defined in (2.1). Since the numerical values of $\mathcal{E}/H\mu$ and $\mathcal{E}$ are identical, for notational simplicity the same symbol $\mathcal{E}$ will be used to denote the dimensionless energy $\mathcal{E}/H\mu$.

For the functionally graded Neo-Hookean structure, the shear modulus exponent in (2.7) used in the calculations is $\alpha = 3$. For the bi-layered structure – Neo-Hookean or power-law – the film-to-layer thickness

[20] With the exception of u_1^s at $X_1 = 0$.

[21] To avoid introducing new notation, the solution whose stability is under investigation has period $L = L_d$ while the perturbations considered are defined over a much larger domain, thus explaining $k \in [0,1)$ – see footnote 11 associated to (2.5).

ratio is $H_f/H = 0.1$ and the film-to-substrate stiffness ratio $\mu_f/\mu_s = 2$. For the power-law material model with $p \geq 1$ (i.e. strain hardening $p = 1.25$ and Neo-Hookean $p = 1$ cases) a Poisson's ratio of $\nu = 0.8182$ is adopted while for $p < 1$ (i.e. strain softening case $p = 0.75$) we use $\nu = 0.3333$ in view of its softer response as seen in Figure 2.

4.1. Principal Solution and its Stability

As discussed in Section 2, the solution of the equilibrium equation (2.2) in the model's fixed-point space is $\overset{0}{\mathbf{u}}(\mathbf{X};\varepsilon) = \mathbf{0} \in \mathcal{S}_{C_{\infty v}}$ (see Appendix A). To determine its stability we must find, according to Subsection 2.2, the minimum eigenvalue $\beta_{min}(\varepsilon)$, with respect to all functions $\boldsymbol{\Delta}\mathbf{u}$ (the unit norm requirement $\|\boldsymbol{\Delta}\mathbf{u}\| = 1$ replacing the inner product $\langle \boldsymbol{\Delta}\mathbf{u}, \boldsymbol{\Delta}\mathbf{u}\rangle$ in the Rayleigh quotient definition of β) according to[22] (2.4)

$$\beta_{min}(\varepsilon) = \min_{\|\boldsymbol{\Delta}\mathbf{u}\|=1} \frac{1}{L_d} \int_{\Omega_d} [(\nabla\boldsymbol{\Delta}\mathbf{u}) : \overset{0}{\mathbf{L}}(X_2;\varepsilon) : (\nabla\boldsymbol{\Delta}\mathbf{u})]\, dA \; ; \quad \forall\boldsymbol{\Delta}\mathbf{u}(\mathbf{X}) = \exp(i2\pi k X_1/L_d)\, \boldsymbol{\delta}\mathbf{u}(X_2) \; ,$$
$$\boldsymbol{\delta}\mathbf{u}(X_2) \; : \; [0,H] \longrightarrow \mathbb{R}^2 \; , \quad k \in [0,1) \; ; \quad \overset{0}{\mathbf{L}} \equiv \frac{\partial^2 W(\mathbf{F};X_2)}{\partial\mathbf{F}\partial\mathbf{F}}\Big|_{\overset{0}{\mathbf{F}}(\varepsilon)} \; . \tag{4.1}$$

Consequently, by substituting (2.5) into $\mathcal{E}^0_{,\mathbf{uu}}$, one obtains the minimum eigenvalue of this operator

$$\beta_{min}(k;\varepsilon) = \min_{\|\boldsymbol{\Delta}\mathbf{u}\|=1} \mathcal{Q}(\boldsymbol{\delta}\mathbf{u},k;\varepsilon) \; , \; k \in [0,1) \; ; \quad \mathcal{Q} \equiv \int_0^H [\overline{(\nabla\boldsymbol{\Delta}\mathbf{u})} : \overset{0}{\mathbf{L}}(X_2;\varepsilon) : (\nabla\boldsymbol{\Delta}\mathbf{u})]\, dX_2 \; , \tag{4.2}$$

where an overline $\overline{f}$ denotes complex conjugation of a quantity f and where $\mathcal{Q}$ is a quadratic function of $\boldsymbol{\delta}\mathbf{u}(X_2;\varepsilon) \equiv (\boldsymbol{\delta}\mathbf{u}^c(X_2;\varepsilon)\cos(2\pi k X_1/L_d) + i\, \boldsymbol{\delta}\mathbf{u}^s(X_2;\varepsilon)\sin(2\pi k X_1/L_d))$ that depends also on the wavenumber k as well as on the load parameter ε. One can easily see that the unstressed configuration $\varepsilon = 0$, $\overset{0}{\mathbf{F}}(0) = \mathbf{I}$ is stable. Indeed the corresponding second derivative of the energy gives the elastic moduli tensor of isotropic linear elasticity $\overset{0}{\mathbf{L}}(X_2;0) = \mathbf{L}^e$ which is convex (positive energy) with respect to the small strain (symmetric part of $(\nabla\boldsymbol{\delta}\mathbf{u})$) and consequently from (4.2) the quadratic form $\mathcal{Q}$ is positive for each nontrivial admissible field $(\nabla\boldsymbol{\delta}\mathbf{u})$.

Of interest is the strain ε_c at the onset of the first bifurcation encountered on the principal solution and the associated eigenmode wavelength L_c, different from the arbitrarily chosen L_d. To this end we proceed as follows: We notice that $\mathcal{Q}$ depends on the dimensionless wavenumber $\omega \equiv 2\pi k H/L_d$ (and hence the corresponding minimum eigenvalue β_{min} has to be calculated[23] for $\omega \in [0,\infty)$. We thus determine from (4.2) the minimum eigenvalue $\beta_{min}(\omega;\varepsilon)$ of the stability operator $\mathcal{Q}(\boldsymbol{\delta}\mathbf{u},\omega;\varepsilon)$ for a given pair $(\omega;\varepsilon)$. We subsequently find $\varepsilon_{min}(\omega)$, the lowest nontrivial ε root of β_{min} for each fixed ω,

$$\beta_{min}(\omega;\varepsilon_{min}(\omega)) = 0 \; ; \quad \beta_{min}(\omega;\varepsilon) > 0 \; , \; 0 \leq \varepsilon < \varepsilon_{min}(\omega) \; , \quad \omega \in \mathbb{R}^+ \; . \tag{4.3}$$

It can be shown that, since $\beta_{min}(\omega;\varepsilon_{min}(\omega)) = 0$, a bifurcated solution emerges from the principal one at each $\varepsilon_{min}(\omega)$ and that from symmetry the corresponding eigenmodes are symmetric, $\boldsymbol{\Delta}\mathbf{u}^s(\mathbf{X}) = [\cos(\omega X_1/H)\delta u_1(X_2),\ \sin(\omega X_1/H)\delta u_2(X_2)]^{\mathrm{T}}$, and asymmetric, $\boldsymbol{\Delta}\mathbf{u}^a(\mathbf{X}) = [-\sin(\omega X_1/H)\delta u_1(X_2),\ \cos(\omega X_1/H)\delta u_2(X_2)]^{\mathrm{T}}$.

Finally, the sought critical (i.e. lowest) bifurcation load ε_c is the infimum of $\varepsilon_{min}(\omega)$ with respect to ω, attained at some[24] ω_c, which also determines the wavelength of the corresponding eigenmode L_c

$$\varepsilon_c \equiv \inf_{\omega\in\mathbb{R}^+} \varepsilon_{min}(\omega) = \varepsilon_{min}(\omega_c) \; ; \quad L_c = 2\pi H/\omega_c \; . \tag{4.4}$$

[22] For the stability of the principal solution, the L_d-periodic function $\mathbf{p}(\mathbf{X})$ in (2.5) depends solely on X_2, i.e. $\mathbf{p}(\mathbf{X}) = \boldsymbol{\delta}\mathbf{u}(X_2)$. Also, here we consider the case where $L_d \to \infty$ and thus take $k \in [0,1)$. See further, Footnote 11.

[23] From the self-adjointness of $\mathcal{E}_{,\mathbf{uu}}$ – also easily checked from (4.1) – one deduces $\beta_{min}(\omega;\varepsilon) = \beta_{min}(-\omega;\varepsilon)$.

[24] The use of infimum in the definition of ε_c is due to a possible singularity at $\omega \longrightarrow 0$, in which case $L_c \longrightarrow \infty$.

For the derivations leading to the analytical calculation of $\varepsilon_{min}(\omega)$, the interested reader in referred to Akerson and Elliott (2021). The reader is also reminded of the discussion in Subsection 2.4, that larger domains $\Omega_d = [-L_d/2, L_d/2] \times [0, H]$ are also considered where $L_d = qL_c$, $q \in \mathbb{N}$ in which case the bifurcation of the principal solution also takes place at ε_c which occurs for $\omega = 2\pi qH/L_d = 2\pi H/L_c = \omega_c$.

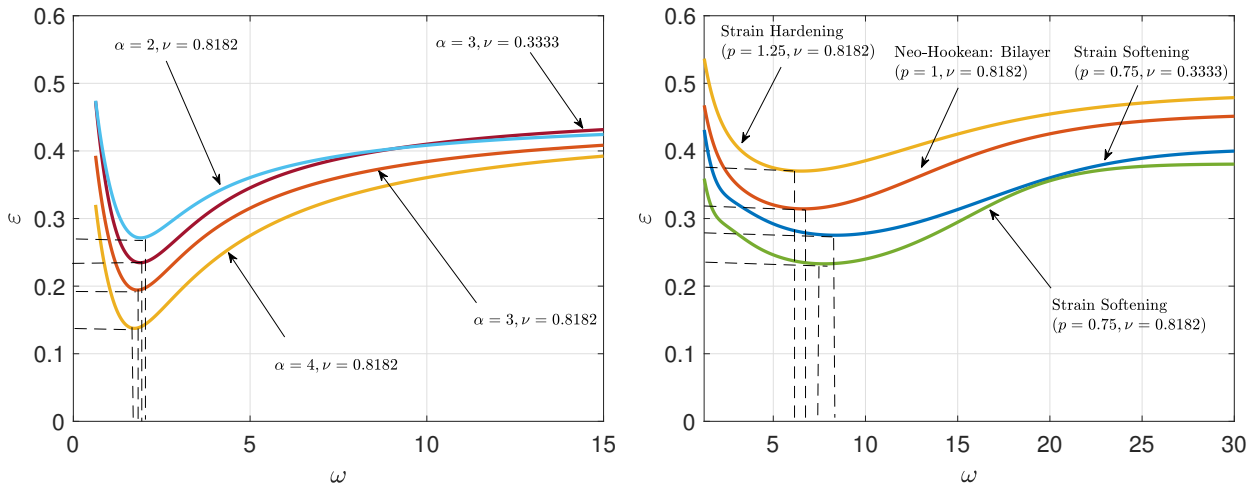

Figure 3: Graph of ε_{min}, the lowest strain corresponding to the first instability on the principal solution, as a function of the dimensionless wavenumber ω for the different structures considered: in (a) functionally graded Neo-Hookean layer ($\alpha = 1,\ 2,\ 3$), and in (b) power-law bi-layer ($H_f/H = 0.1,\ \mu_f/\mu_s = 2$) for three different power-law exponents ($p = 1.25,\ 1.00,\ 0.75$) and two different compressibilities ($\nu = 0.8182,\ 0.3333$).

Figure 3 shows the dependence of ε_{min}, the lowest strain corresponding to the first instability of the principal solution – defined in (4.3) – as a function of the dimensionless wavenumber ω for the different structures considered: functionally graded Neo-Hookean in Figure 3a, and bi-layer in Figure 3b ($H_f/H = 0.1,\ \mu_f/\mu_s = 2$) for three different power-law exponents ($p = 1.25,\ 1.00,\ 0.75$) and two different compressibilities ($\nu = 0.8182,\ 0.3333$). According to the results in Figure 3a, as the grading exponent α increases, i.e. as the material is progressively stiffening near the free surface, the critical strain ε_c decreases. This confirms the results of Akerson and Elliott (2021). For the bi-layer structures, the results of Figure 3b show that the critical strain ε_c decreases with the decreasing stiffness of the material, i.e. as its power-law p exponent decreases. For a given power-law exponent, the critical strain is higher for the more compressible material, as seen in Figure 3b by comparing the $\varepsilon_{min}(\omega)$ curves for the layered structures with $p = 0.75,\ \nu = 0.8182$ and $p = 0.75,\ \nu = 0.3333$.

For the functionally graded layer, the corresponding critical wavenumber $\omega_c \approx 2$, is rather insensitive to the grading exponent and the Poisson ratio. In contrast, for the bi-layer case the critical wavenumber ω_c shows a stronger dependence on the constitutive law, ranging approximately in the interval $6 \leq \omega_c \leq 8$. The lower value of the critical wavenumber for the graded layer – compared to the bi-layers – can be explained by the fact that the instability phenomena are occurring within a thin zone near the free surface. Note that in all cases examined in Figure 3, the critical strain reaches an asymptote for large values of ω, as the corresponding instability mode is Biot's exponentially decaying surface mode of an infinite halfspace with the same properties as the surface (film) layer. The consequence of this observation, which explains the mesh-dependence of the numerical results at localized deformations, is discussed in Appendix C.

4.2. Primary Bifurcation Orbit and its Stability

We focus next on the primary bifurcation orbits, i.e. the initially *uniformly wrinkled* periodic configuration solutions of the layered system. These paths emerge from the lowest critical load ε_c, where a double, pitchfork

bifurcation occurs. At this point a continuous orbit of bifurcated equilibrium paths can be constructed starting from any linear combination of the eigenmodes: $a\Delta\mathbf{u}^s(\mathbf{X}) + b\Delta\mathbf{u}^a(\mathbf{X})$. A representative element of this orbit that also belongs to the fixed-point space $\mathcal{S}_{C_{rv}}$ (see Appendix A), is the L_c-periodic solution $\overset{1}{\mathbf{u}}(\mathbf{X};\varepsilon)$, plotted in Figure 4, and parameterized using the bifurcation amplitude ξ, defined as the absolute value of the X_2-displacement of the free surface at $X_1 = 0$: $\xi \equiv |u_2(0, H)|$. The reason for this choice[25] is that the applied axial strain $\varepsilon(\xi)$ is not a monotonic function of ξ.

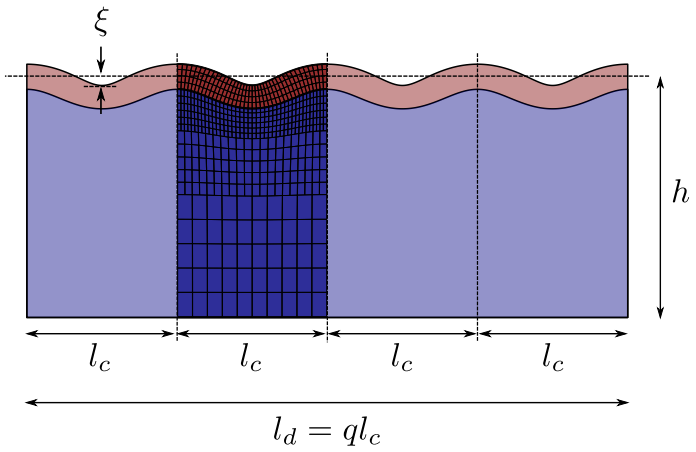

Figure 4: Deformed (current) configuration $(\mathbf{x}(\mathbf{X};\varepsilon(\xi)) = \overset{0}{\mathbf{F}}(\varepsilon)\cdot\mathbf{X} + \overset{1}{\mathbf{u}})$ corresponding to the primary bifurcated equilibrium path $\overset{1}{\mathbf{u}}(\mathbf{X};\xi)$ is an $l_c \equiv (1-\varepsilon_c)L_c$-periodic function, where the bifurcation amplitude parameter ξ, is defined as the absolute value of the X_2-displacement of the free surface at $X_1 = 0$. The unit cell solution is calculated on half of the diagonally hatched domain and completed by symmetry over the super-cell domain in the current configuration. The Neo-Hookean bi-layer model $(\mu_f/\mu_s = 2,\ H_f/H = 0.1)$ result shown here is a representative of the continuous orbit of the C_{rv}-symmetric bifurcated paths emerging at ε_c given in Figure 3. The FEM mesh is indicated on one full ℓ_c period.

Taking advantage of symmetry, as discussed in Section 3, the resulting deformed configuration is obtained by solving the equilibrium equations in (2.2) over half its unit cell domain $\Omega_c^* = [0,\ L_c/2]\times[0,\ H]$. A typical deformed configuration – here for a Neo-Hookean bi-layer model with $\mu_f/\mu_s = 2,\ H_f/H = 0.1$ – is plotted in Figure 4. The unit cell solution is calculated on half of the shown meshed region and completed by symmetry over the super-cell domain in the current configuration $[(l_d = \lambda_1(\varepsilon)L_d)\times(h = \lambda_2(\varepsilon)H)]$, with $L_d = 4L_c$; the dashed line gives the surface location of the principal solution. The same figure depicts the typical FEM mesh used in the numerical calculations and shows the mesh refinement used near the free surface, due to the expected localization of the deformation pattern in that region.

The primary bifurcation orbits $\overset{1}{\mathbf{u}}(\mathbf{X};\varepsilon)$ emerging from the principal solution $(\overset{0}{\mathbf{u}}(\mathbf{X};\varepsilon) = \mathbf{0})$ for four – one graded and three different bi-layered – of the structures studied in Figure 3 are plotted in Figure 5, where the left and right columns show respectively results for the functionally graded and bi-layer structures. Figures 5a, 5b show the amplitude ξ vs. strain ε, Figures 5c, 5d show energy change $(\mathcal{E}-\mathcal{E}^0)$ vs. strain ε, and Figures 5e, 5f show axial force change $(\mathcal{E}-\mathcal{E}^0)_{,\varepsilon}$ vs. strain ε. The stability of the primary bifurcation orbits, based on Bloch wave calculations of a L_c unit cell – as described in Subsection 2.2 – is also recorded using solid and dot-dashed lines, respectively, for the stable and unstable parts of these orbits. The computation along each path is terminated (indicated by a black "x" in the figures) somewhat before self contact occurs to avoid presentation of misleading results. (Beyond these points the accuracy of the employed contact model becomes less reliable, and there are mesh-dependence concerns since the computed creased configuration is of the same length-scale as the FEM mesh.)

[25] In fact, even the employed parameterization is problematic, since it is restricted to $\xi \geq 0$, and is therefore unable to distinguish between the two "halves" of the bifurcated path.

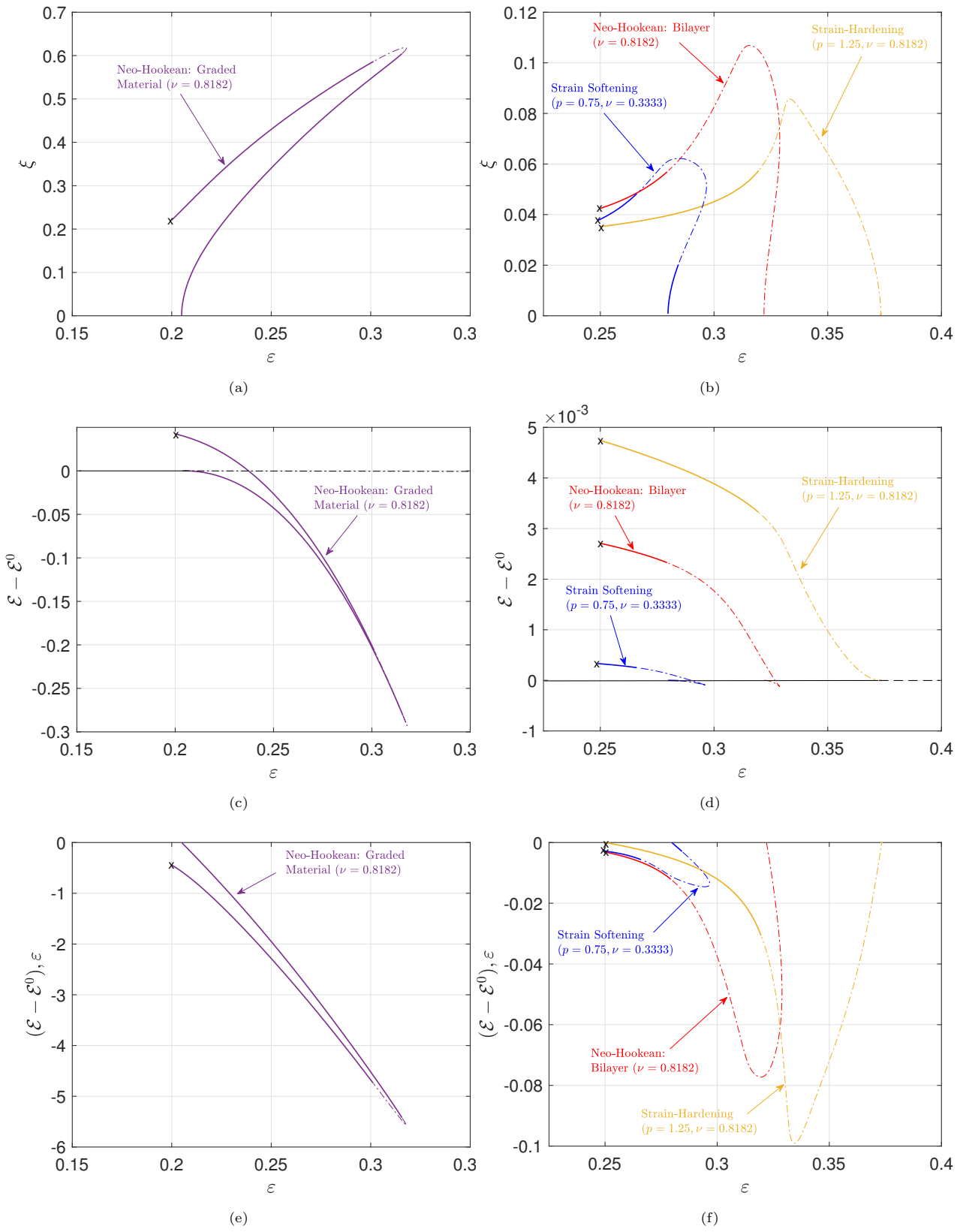

Figure 5: Plots showing the emergence of the primary bifurcation orbit $\overset{1}{\mathbf{u}}(\mathbf{X};\varepsilon)$ from the principal solution $(\overset{0}{\mathbf{u}}(\mathbf{X};\varepsilon) = \mathbf{0})$ for the different types of structures considered: graded Neo-Hookean ($\alpha = 3$, left column), and bi-layered ($H_f/H = 0.1,\ \mu_f/\mu_s = 2$ for three different power-law models, right column). Bifurcation diagrams show: in top row (a) and (b) amplitude ξ vs. strain ε, in middle row (c) and (d) energy change $(\mathcal{E} - \mathcal{E}^0)$ vs. strain ε and in bottom row (e) and (f) lateral force change $(\mathcal{E} - \mathcal{E}^0)_{,\varepsilon}$ vs. its work-conjugate strain ε. Solid and dot-dashed lines correspond, respectively, to the stable and unstable parts of the primary bifurcation orbit, based on Bloch-wave analysis of a L_c unit cell.

Material property grading plays an important role in the nature of the primary bifurcation orbit, as discussed by Akerson and Elliott (2021). As seen in Figure 5a the bifurcation orbits for the graded Neo-Hookean structure are "*supercritical*," i.e. they start with an initial positive curvature at $\varepsilon_c \approx 0.2$. According to the general theory for elastic systems (e.g. see Triantafyllidis and Peek (1992)), the supercritical orbit is initially stable. The bifurcation amplitude increases under increasing strain up until a maximum strain $\varepsilon \approx 0.32$ is reached. Just before the maximum strain the solution becomes unstable and, following a maximum amplitude, experiences a sharp *snap-back* and quickly regains its stability.

A creased (strongly localized deformation) pattern is associated with this snap-back part of the $\varepsilon(\xi)$ curve and the term is used hereinafter for the part of the equilibrium orbits beyond their turning points. Typical localized deformed configurations associated with these orbits are illustrated in Figures 11c and 12c. According to Figures 5c, 5d the primary bifurcation orbits have initially a lower energy than the corresponding principal solution at the same applied strain ε. The applied lateral force drops, relative to the flat configuration, when one moves away from the bifurcation point, as seen by Figures 5e, 5f. Also notice that for a given strain ε the bifurcation amplitude of the snap-back part and the energy are higher while the lateral force is lower than in the corresponding part of the path emerging from ε_c.

The initial post-bifurcation behavior for the selected material property (shear modulus) grading exponent ($\alpha = 3$) is in agreement with the asymptotic analysis in Akerson and Elliott (2021). It is noteworthy that the functionally graded Neo-Hookean layer exhibits a primary bifurcation orbit with a maximum axial strain significantly higher than ε_c. The stable, snap-back solution exists for strains lower than ε_c and exhibits a localized deformation pattern, but this does not occur in a neighborhood of ε_c as seen from the bifurcation diagrams of Figure 5.

For the bi-layer structure, the choice of constitutive law has a significant impact on the nature of the primary bifurcation orbits. The strain softening bi-layer ($p < 1$) has a supercritical bifurcation, while the strain hardening bi-layered structure ($p = 1.25$) has a subcritical orbit, i.e. the strain is reduced as the bifurcation amplitude increases. The Neo-Hookean bi-layer ($p = 1$) primary bifurcation orbit emerges as subcritical and hence unstable at the onset of bifurcation, as seen in Akerson and Elliott (2021), who investigated a Neo-Hookean bi-layer structure as a function of the film/substrate stiffness ratio μ_f/μ_s.

With the exception of a small neighborhood near ε_c for the strain softening bi-layer, all bifurcated orbits are unstable and remain so well beyond all their turning points, until the stable branch of the snap-back is reached. Notice nevertheless the somewhat counter-intuitive result that the strain softening bi-layer exhibits a primary bifurcation orbit with a maximum axial strain higher than ε_c, while its strain stiffening counterpart has a post-bifurcated orbit with an applied strain monotonically decreasing away from ε_c. Once again from Figure 5, the stable, snap-back solutions with a localized deformation pattern exist for strains lower than ε_c but well away from a neighborhood of ε_c.

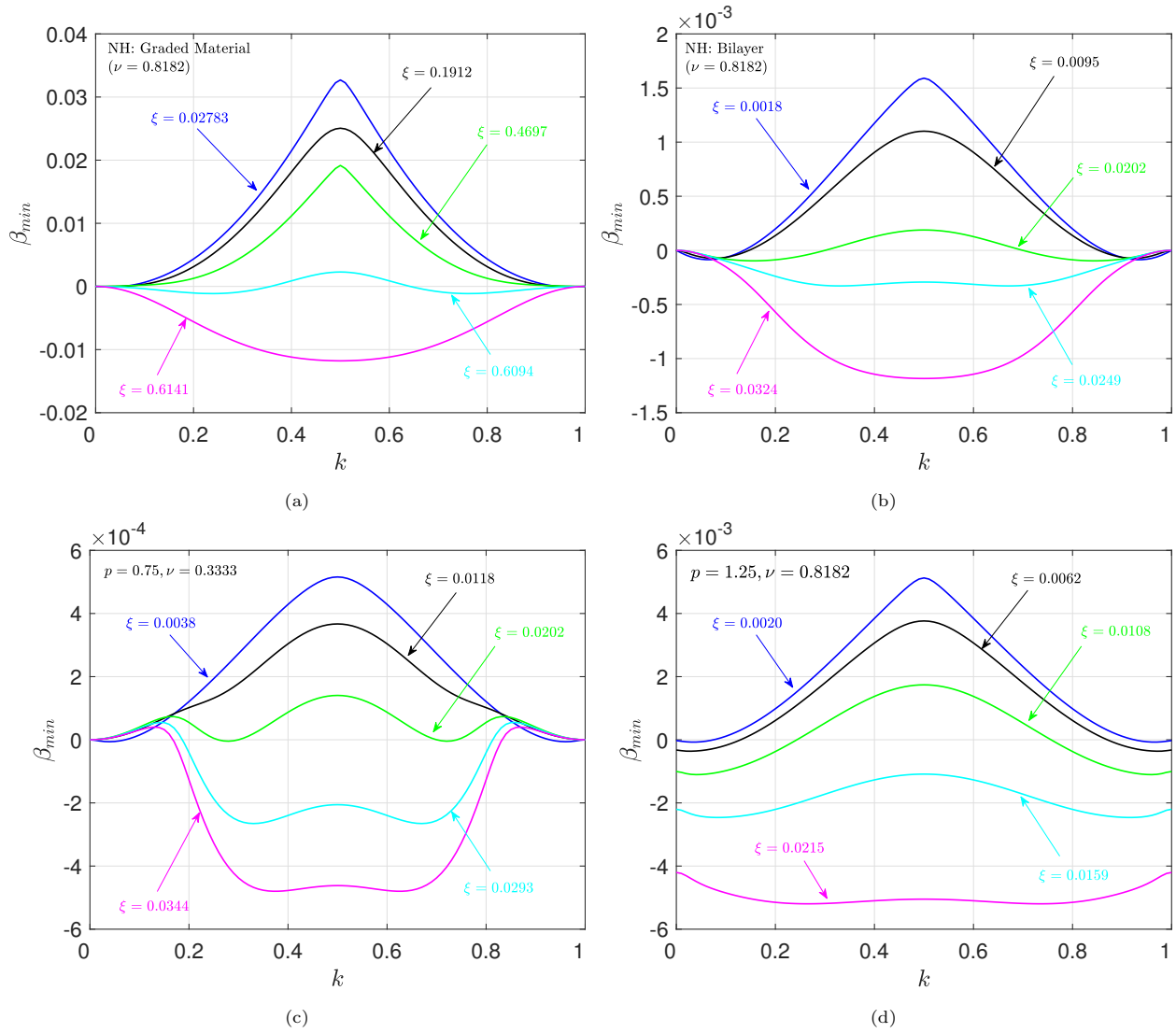

Figure 6: Dispersion relations – minimum eigenvalue of the stability operator $\beta_{min}(k)$ vs. wavenumber k – at different bifurcation amplitudes ξ for the primary bifurcation paths of the four different structures: (a) functionally graded Neo-Hookean ($\alpha = 3$), b) bi-layer with Neo-Hookean material $p = 1.00,\ \nu = 0.8182$, (c) bilayer with strain softening material $p = 0.75,\ \nu = 0.3333$ and (d) bi-layer with strain hardening material $p = 1.25,\ \nu = 0.8182$.

Based on the numerical procedure described in Section 3, a more detailed picture of the stability of the primary bifurcation orbit $\overset{1}{\mathbf{u}}(\mathbf{X};\varepsilon)$ is provided by a plot of the minimum eigenvalue $\beta_{min}(k)$ as a function of the wavenumber k; such plots are commonly referred to as a "*dispersion relation.*"[26] Here, on a single plot, we present multiple dispersion relations at different values of the bifurcation amplitude ξ along the primary bifurcated equilibrium path. In Figure 6a are presented the dispersion curves for the functionally graded Neo-Hookean ($\alpha = 3$) layer and Figures 6b, 6c and 6d, respectively, show the corresponding dispersion curves for the bi-layer with the three different power-law materials: $p = 1.00,\ \nu = 0.8182$, $p = 0.75,\ \nu = 0.3333$, and $p = 1.25,\ \nu = 0.8182$.

[26]However, this is really an abuse of the term which originates in the theory of waves and properly describes the temporal frequency versus wavenumber curve.

Since the stability operator $\mathcal{E}_{,\mathbf{uu}}$ is self-adjoint, the eigenvalues of the corresponding discretized Hermitian stiffness matrix are real and symmetric with respect to $k = 0$, i.e. $\beta_{min}(k) = \beta_{min}(-k)$. This property, combined with the periodicity of the eigenvalue, i.e. $\beta_{min}(k+1) = \beta_{min}(k)$, following from (3.5), results in the mirror symmetry of the graphs in Figure 6 with respect to $k = 1/2$. Their intersection with the $\beta_{min} = 0$ line indicates bifurcation points.

A curve lying entirely above the k-axis means that the orbit in question, identified by its bifurcation amplitude, is stable. As expected from the results in Figures 5a, 5b, where the post bifurcation behavior for the functionally graded structure and the strain softening bi-layer are supercritical, for small values of the bifurcation amplitude ξ the corresponding dispersion curves lie entirely above the k-axis, as seen in Figures 6a and 6c. As the bifurcation amplitude increases, the orbits in each structure become unstable and the corresponding dispersion curves dive below the k-axis, as all orbits become unstable until a significant crease is formed and they regain their stability.[27]

Finally a remark is in order about the existence of $\beta_{min}(0) = 0$ in the above dispersion curves. At $k = 0$, as seen in the Figure 6 graphs $\beta_{min} = 0$ for the principal solution ($\xi = 0$), while $\beta = 0$ is an eigenvalue for the primary bifurcation orbits ($\xi > 0$), but not necessarily the minimum one. The reason stems from the fact that the stability operator $\mathcal{E}_{,\mathbf{uu}}$ evaluated on any solution of the equilibrium equations which is L_d-periodic – and hence corresponding to $k = 0$ according to (3.5) – can be shown to have a zero eigenvalue. Indeed differentiating the equilibrium equations for an equilibrium solution $(\mathcal{E}_{,\mathbf{u}}(\mathbf{u}(X_1 + c, X_2); \varepsilon), \delta\mathbf{u}) = 0$ with respect to an arbitrary phase-shift $c(\theta)$ (see (2.10)) we obtain

$$\frac{d}{dc}(\mathcal{E}_{,\mathbf{u}}(\mathbf{u}(X_1 + c, X_2); \varepsilon), \delta\mathbf{u}) = 0 \quad \Longrightarrow \quad ((\mathcal{E}_{,\mathbf{uu}}, [\frac{\partial \mathbf{u}}{\partial X_1}(X_1, X_2; \varepsilon)]), \delta\mathbf{u}) = 0 \,, \tag{4.5}$$

indicating that zero is an eigenvalue of the stability operator $\mathcal{E}_{,\mathbf{uu}}$ with corresponding eigenmode $\partial\mathbf{u}/\partial X_1$.

4.3. Secondary Bifurcation Orbits

We are interested next in the secondary bifurcation orbits emerging from the primary ones presented above. Once again, due to symmetry, as discussed in Section 3 equilibrium solutions are computed on the domain $\Omega_d^* = [0, L_d/2] \times [0, H]$, while the stability analysis of the resulting orbits is based on the domain $\Omega_d = [-L_d/2, L_d/2] \times [0, H]$, where $L_d = 4L_c$. The results for all the structures analyzed – and whose primary orbits appear in Figure 5 – are now presented in Figures 7 to 10. More specifically, the secondary orbit graphs presented in Figure 7 show the amplitude ξ vs. strain ε, in Figure 8 the energy change $(\mathcal{E} - \mathcal{E}^0)$ vs. strain ε and in Figure 9 the force change $(\mathcal{E} - \mathcal{E}^0)_{,\varepsilon}$ vs. amplitude ξ. All bifurcation points are indicated by a small circle, while solid and dot-dashed lines correspond, respectively, to the stable and unstable parts of these equilibrium paths. In Figure 10 deformed configurations are plotted at selected points, indicated in Figures 7 to 9. Colors show the absolute value of the Lagrangian strain's shear component $|E_{12}|$, chosen as a measure of the localized deformation in view of the absence of shear in the principal solution ($\overset{0}{\mathbf{F}}(\varepsilon) = \mathrm{diag}[\lambda_1(\varepsilon), \lambda_2(\varepsilon)] \implies \overset{0}{E}_{12} = 0$).

[27] Dispersion curves for adequately large amplitudes, corresponding to restabilized orbits, are not depicted in Figure 6.

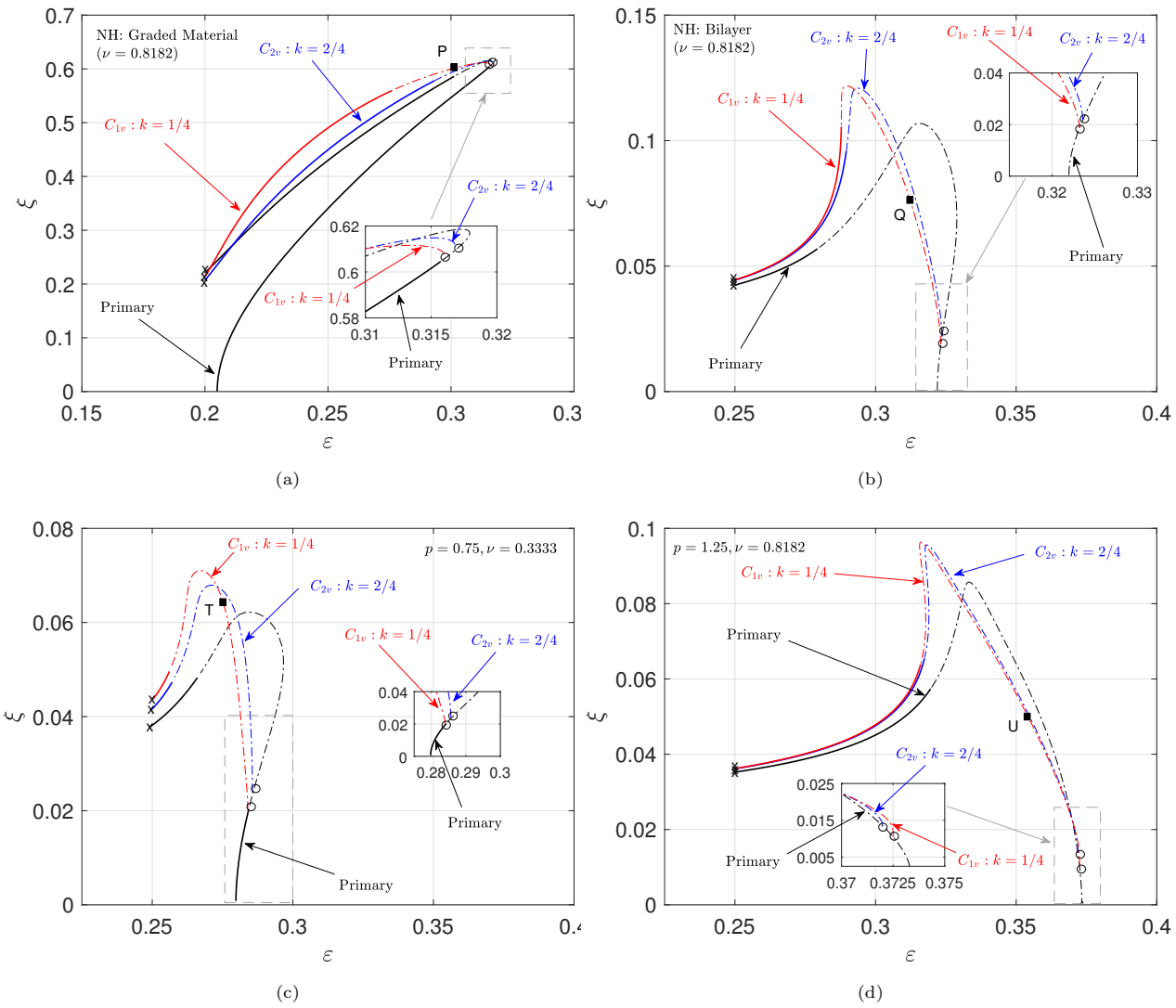

Figure 7: Amplitude ξ vs. applied strain ε graphs of the secondary bifurcation orbits for the: (a) functionally graded Neo-Hookean layer ($\alpha = 3$), (b) Neo-Hookean ($p = 1.00,\ \nu = 0.8182$) bi-layer ($H_f/H = 0.10,\ \mu_f/\mu_s = 2$), (c) strain softening material ($p = 0.75,\ \nu = 0.3333$) bi-layer ($H_f/H = 0.10,\ \mu_s/\mu_f = 2$) and (d) strain hardening material ($p = 1.25,\ \nu = 0.8182$) bi-layer ($H_f/H = 0.10,\ \mu_s/\mu_f = 2$).

As seen from Figure 7a, the secondary bifurcation orbits for the exponentially graded material ($\alpha = 3$) emerge near $\varepsilon = 0.316$, just prior to the primary path reaching its turning point, a significantly higher value than the critical strain $\varepsilon_c = 0.205$. In contrast, the secondary bifurcation orbits of the bi-layers emerge at strains near the corresponding critical ones, as seen from Figures 7b, 7c and 7d. A common feature in all cases is that the orbit corresponding to $k = 1/4$ (period-quadrupling) mode emerges first and leads to an initially unstable secondary bifurcated orbit with C_{1v} symmetry, followed by another initially unstable secondary orbit with C_{2v} symmetry corresponding to the $k = 1/2$ (period-doubling) mode.

Both of these secondary bifurcated orbits evolve to a solution with a highly localized deformation pattern at the surface as the overall strain ε decreases and the bifurcation amplitude ξ keeps increasing along these paths, until a maximum amplitude is reached. As with the primary bifurcation orbits presented in Figure 5, the counter-intuitive decrease in the bifurcation amplitude in the secondary bifurcation orbits, is due to the decrease in the overall lateral expansion of the layer (recall $h = \lambda_2(\varepsilon)H$) caused by the decreasing strain ε.

In all cases of Figure 7, for a given strain ε the longer wavelength orbit ($k = 1/4$) has initially – and until close to its turning point – a lower amplitude ξ than its shorter wavelength counterpart ($k = 1/2$).

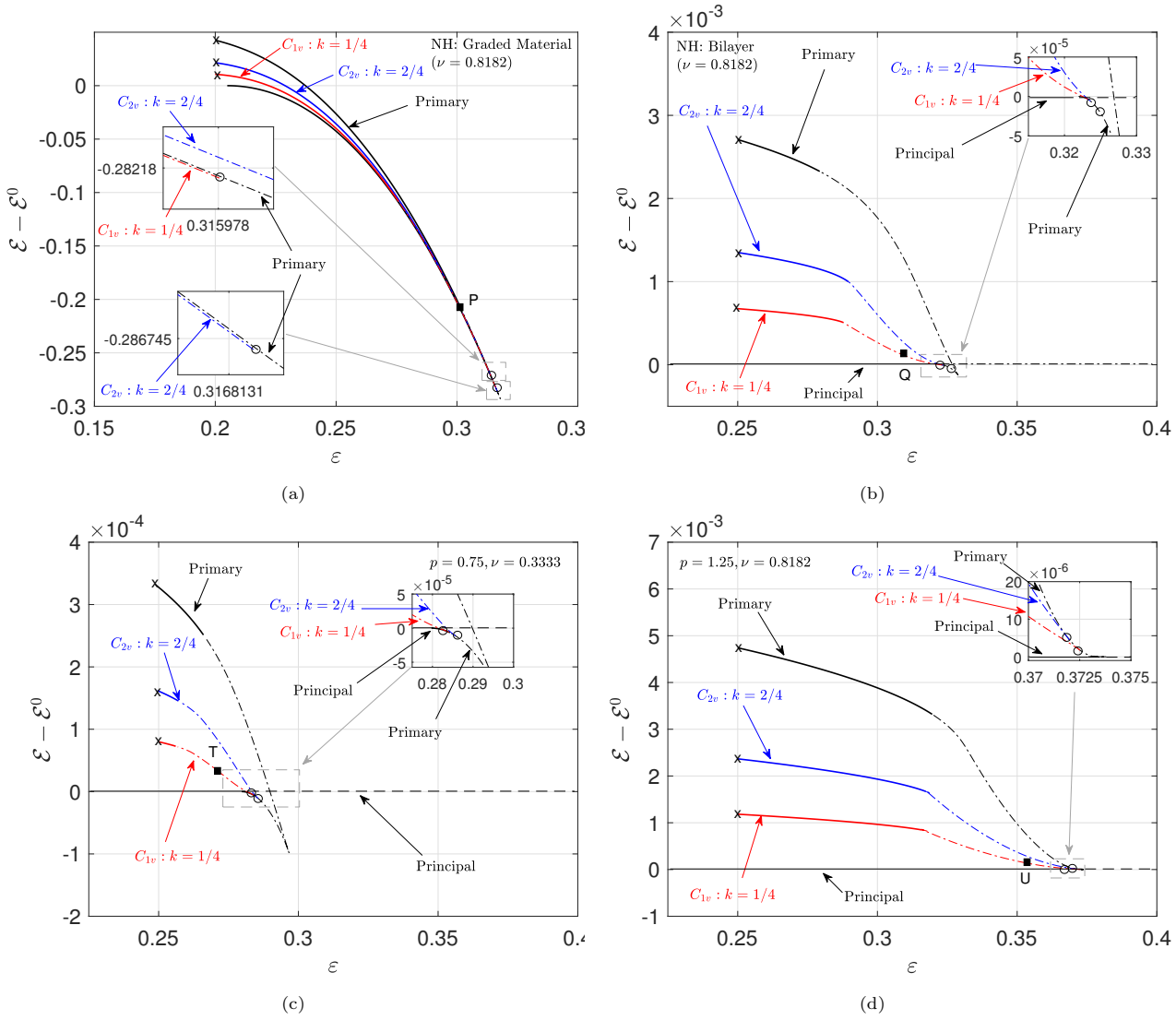

Figure 8: Energy change $\mathcal{E} - \mathcal{E}^0$ vs. applied strain ε graphs of the secondary bifurcation orbits for the: (a) functionally graded Neo-Hookean layer ($\alpha = 3$), (b) Neo-Hookean ($p = 1.00,\ \nu = 0.8182$) bi-layer ($H_f/H = 0.10,\ \mu_f/\mu_s = 2$), (c) strain softening material ($p = 0.75,\ \nu = 0.3333$) bi-layer ($H_f/H = 0.10,\ \mu_s/\mu_f = 2$) and (d) strain hardening material ($p = 1.25,\ \nu = 0.8182$) bi-layer ($H_f/H = 0.10,\ \mu_s/\mu_f = 2$).

The energy change $\mathcal{E} - \mathcal{E}^0$ vs. strain ε results are shown in Figure 8. A common feature shared by all cases studied is that the secondary bifurcation orbit corresponding to $k = 1/4$ (which has a C_{1v} symmetry) has a lower energy than the C_{2v} symmetry orbit corresponding to $k = 1/2$. As one follows these orbits away from their emergence on the primary orbit, the applied strain ε decreases but the difference between the energies of the principal and secondary orbits continue to increase, with the C_{1v} symmetry orbit having the lowest energy among all identified bifurcated solutions.

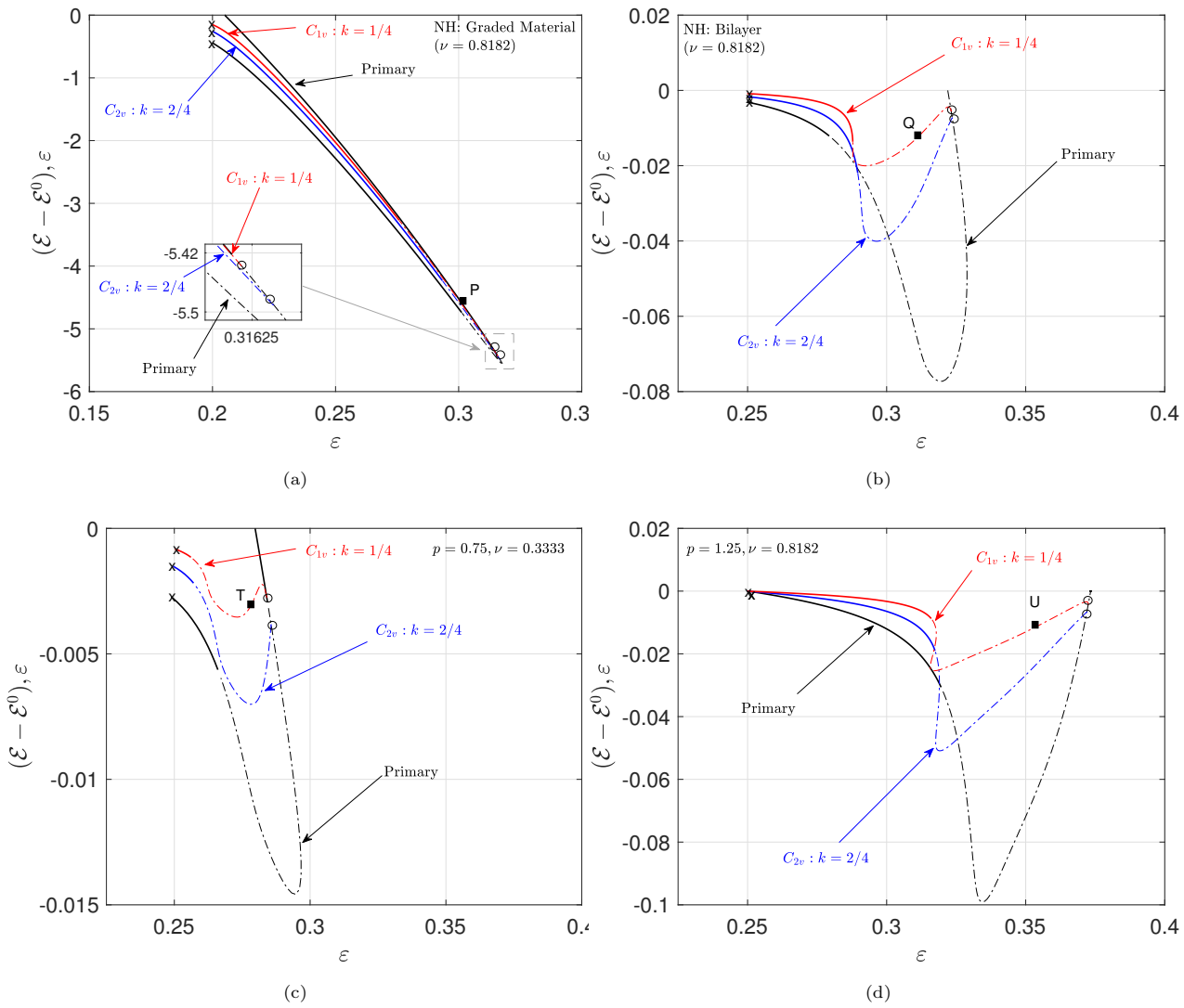

Figure 9: Force change $(\mathcal{E} - \mathcal{E}^0)_{,\varepsilon}$ vs. applied strain ε graphs of the secondary bifurcation orbits for the: (a) functionally graded Neo-Hookean layer ($\alpha = 3$), (b) Neo-Hookean ($p = 1.00,\ \nu = 0.8182$) bi-layer ($H_f/H = 0.10,\ \mu_f/\mu_s = 2$), (c) strain softening material ($p = 0.75,\ \nu = 0.3333$) bi-layer ($H_f/H = 0.10,\ \mu_s/\mu_f = 2$) and (d) strain hardening material ($p = 1.25,\ \nu = 0.8182$) bi-layer ($H_f/H = 0.10,\ \mu_s/\mu_f = 2$).

The lateral force change $(\mathcal{E} - \mathcal{E}^0)_{,\varepsilon}$ results are plotted in Figure 9. An analogous observation can be made with the results of Figure 8 showing the energy difference $(\mathcal{E} - \mathcal{E}^0)$ versus bifurcation amplitude ξ: the secondary bifurcation orbit corresponding to $k = 1/4$ (which has a C_{1v} symmetry) has a lower lateral force than the C_{2v} symmetry orbit corresponding to $k = 1/2$. As one follows these orbits away from their emergence on the primary orbit, the applied strain ε decreases but the difference between the lateral forces of the principal and secondary orbits continue to increase, with the C_{1v} symmetry orbit having the lowest lateral force change.

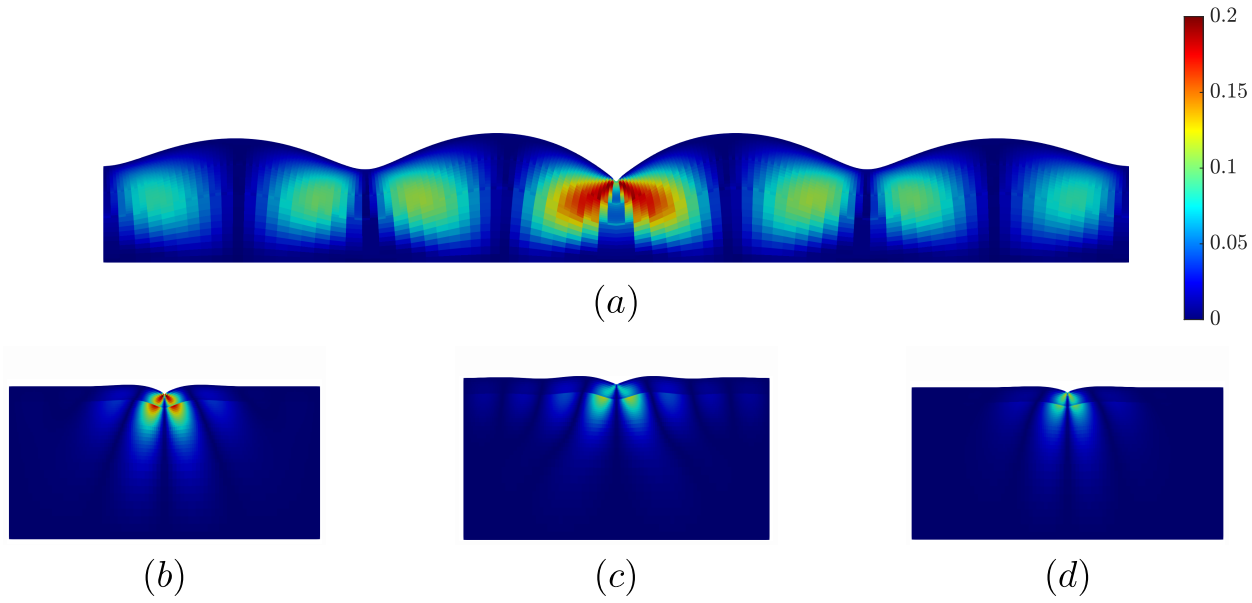

Figure 10: Deformed configuration with contours for the absolute value of the Lagrangian strain shear component $|E_{12}|$ of the secondary bifurcation orbit with C_{1v}-symmetry, corresponding to the $k = 1/4$ bifurcation mode for: (a) the functionally graded layer ($\alpha = 3$) at point P, (b) the Neo-Hookean ($p = 1.00,\ \nu = 0.8182$) bi-layer at point Q, (c) the strain softening material ($p = 0.75,\ \nu = 0.3333$) bi-layer at point T and (d) strain hardening material ($p = 1.25,\ \nu = 0.8182$) bi-layer at point U (see Figures 7, 8 and 9, respectively).

Deformed configurations with contours for the absolute value of the Lagrangian strain shear component $|E_{12}|$ are presented for selected points along the secondary bifurcation orbit with C_{1v}-symmetry (corresponding to the $k = 1/4$ bifurcation mode) for: (a) the functionally graded layer ($\alpha = 3$) at point P, (b) the Neo-Hookean ($p = 1.00,\ \nu = 0.8182$) bi-layer at point Q, (c) the strain softening material ($p = 0.75,\ \nu = 0.3333$) bi-layer at point T and (d) stiffer material ($p = 1.25,\ \nu = 0.8182$) bi-layer at point U (see Figures 7, 8, 9). Moreover, similarly to the primary bifurcation orbits in Figure 5, the stable secondary bifurcation orbits exhibit a localized deformation pattern and can be found at strains lower than ε_c. However, as seen in Figures 7, 8, 9, this happens far from the neighborhood of ε_c, thus repudiating the idea that these are "*local bifurcations*."

Some interesting comparisons can be made at this point with the structural model (beam on a nonlinear elastic foundation) of Pandurangi et al. (2020) which served as an analytically tractable alternative to the bi-layer continuum model considered here. Although significant differences exist (linearly elastic beam for the film, nonlinear spring model for the substrate), interesting analogies can be found with the onset of the different bifurcation orbits as the symmetry group of the bi-layer model presented here is a proper subgroup of the structural model's counterpart. Moreover, in both cases highly localized stable deformations are found far away from and well below the initial critical load. Both models share a (finite wavelength) periodic primary bifurcation orbit, from which subsequently emerge lower symmetry orbits (secondary, tertiary, etc.).

One interesting difference is that in the structural model the softening(stiffening) foundation results in a unstable(stable), subcritical(supercritical) bifurcation while the opposite is true for the continuum bilayer. As in the structural model, the secondary bifurcation orbit that appears first corresponds to the longest wavelength eigenmode. As for the structural model, for the structure with the subcritical primary orbit, the secondary one will emerge as close to the critical load as the size q of the supercell domain considered increases ($L_d = qL_c$). In the neighborhood of the first primary bifurcation point our results are in agreement with the structural model of Pandurangi et al. (2020).

More broadly, it is interesting to note that, for the current problem all the bifurcated solutions have higher energy than the principal flat solution. Further, the paths all evolve into highly localized configurations that

have very shallow penetration of the free surface into the depth of the strip. Accordingly, once the solution fully localizes the equilibrium corresponds to a mostly homogeneous one with a shallow "*crease*" or "*fold*". The energy of such configurations will be that of the flat uniform principal solution plus a relatively small additional energy due to the surface perturbations. As such, there is little reason to argue that the flat principal configuration would spontaneously transition to the higher-energy shallow localized configurations found in this work. This does not mean that the imperfection-free path-following methods used here are not capable of discovering the deeply penetrating crease and fold configurations of interest. This issue is explored next.

4.4. Development of Creases and Folds – Influence of Material Properties

For the constitutive parameters studied in the previous subsections, the path-following bifurcation method – which does not use imperfections – does not lead to the deeply penetrating creases and folds that have been of considerable interest in the literature, such as those studied by Diab et al. (2013) and coworkers. However, here we show that the details of the evolution of a bifurcated equilibrium path emerging from the principal (flat) configuration into a crease or fold depend strongly on the constitutive properties of the structure (film-to-substrate stiffness ratio μ_f/μ_s and Poisson's ratio ν). In particular, we find that deep creases and folds are, indeed, found via imperfection-free path-following for certain material parameters. Although the first dependence (μ_f/μ_s) is discussed in the literature, the latter (ν) has not been the object of attention since most of the work in this area pertains to incompressible materials.

As discussed in Appendix C, for large values of the bifurcation amplitude ξ, the bifurcation orbits and the details of the localization patterns are mesh-sensitive. Having established that for a large enough sample ($L_d = qL_c,\ q > 1$) the localized deformation with the lowest energy is obtained from the secondary bifurcation orbit that emerges first from the primary one, in the interest of reducing computation time, we study the constitutive influence on the development of creases and folds using the lowest size domain (one cell, $L_d = L_c,\ q = 1$) but with the densest mesh reported in Appendix C.

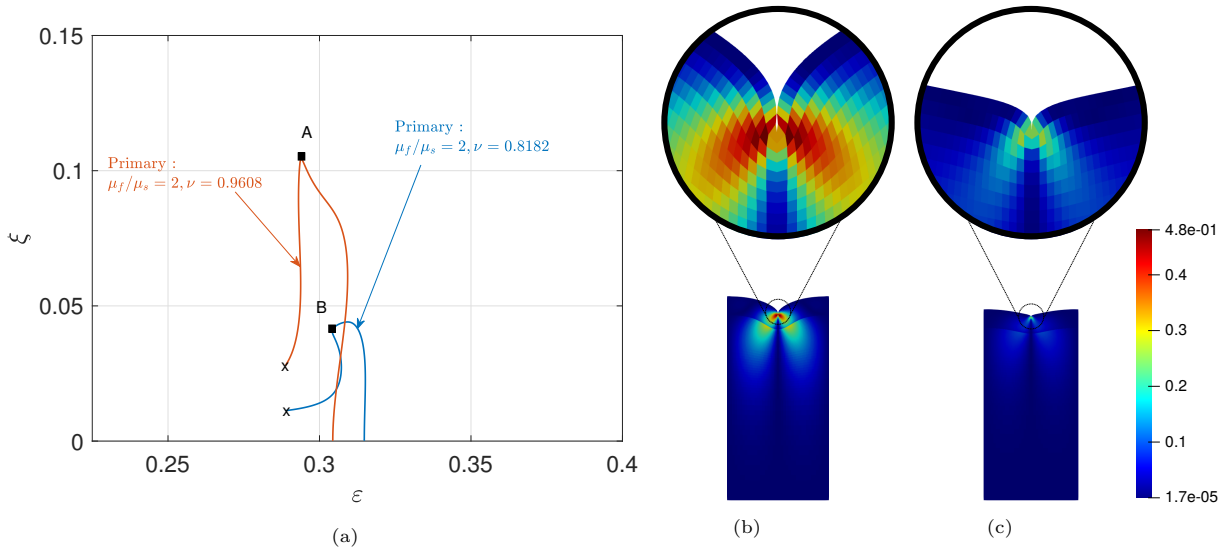

Figure 11: Influence of Poisson's ratio ν on the evolution of the localized deformation pattern. In (a) primary bifurcation orbit, plotted in ε vs. ξ, for a Neo-Hookean bilayer ($H_f/H = 0.1$, $\mu_f/\mu_s = 2$) for two different compressibility values: $\nu = 0.8182$ (see also Figure 5b) and $\nu = 0.9608$. In (b) the localized deformation pattern (fold) for the nearly incompressible $\nu = 0.9608$ case plotted at point A. In (c) the localized deformation pattern for the compressible (crease) $\nu = 0.8182$ case plotted at point B. Deformed configurations also show contours for the absolute value of the Lagrangian strain shear component $|E_{12}|$.

The influence of Poisson's ratio ν on the evolution of the localized deformation pattern is presented in

Figure 11. In Figure 11a we plot[28] the primary bifurcation orbit in ε vs. ξ, for a Neo-Hookean bilayer ($H_f/H = 0.1$, $\mu_f/\mu_s = 2$) for two different Poisson's ratio values: $\nu = 0.8182$ (see also Figure 5b) and $\nu = 0.9608$. Notice that as incompressibility is approached, the maximum bifurcation amplitude ξ reached before snap-back shows a significant increase. Moreover, one can also observe in Figure 11b that the localized deformation pattern for the nearly incompressible $\nu = 0.9608$ case, plotted at point A – maximum bifurcation amplitude – is a small fold while in Figure 11c, the localized deformation pattern for the slightly compressible $\nu = 0.8182$ case, plotted at point B, corresponds to a very small crease.

The transition from crease to fold is made more clear in Figure 12 that pertains to the influence of film-to-substrate stiffness ratio μ_f/μ_s on the evolution of the localized deformation pattern. In Figure 12a we plot ε vs. ξ the primary bifurcation orbit for a nearly incompressible Neo-Hookean bilayer ($H_f/H = 0.1$, $\nu = 0.9608$) for three different values of the stiffness ratio: $\mu_f/\mu_s = 2$ (see also Figure 11a) and $\mu_f/\mu_s = 5,\ 10$. Notice that as the stiffness ratio μ_f/μ_s increases, the maximum bifurcation amplitude ξ reached before snap-back shows a significant increase, while the critical strain ε_c decreases. In addition, we observe in Figure 12b that the localized deformation pattern for the $\mu_f/\mu_s = 10$ case, plotted at maximum bifurcation amplitude ξ and maximum applied strain ε in point C, is a very well-developed, deep fold. In Figure 12c we also find that the localized deformation pattern for the $\mu_f/\mu_s = 5$ case, plotted again at maximum bifurcation amplitude ξ and maximum applied strain ε in point D, is also a fold, although less pronounced than for the $\mu_f/\mu_s = 10$ case, in agreement with existing literature (see Diab et al. (2013)).

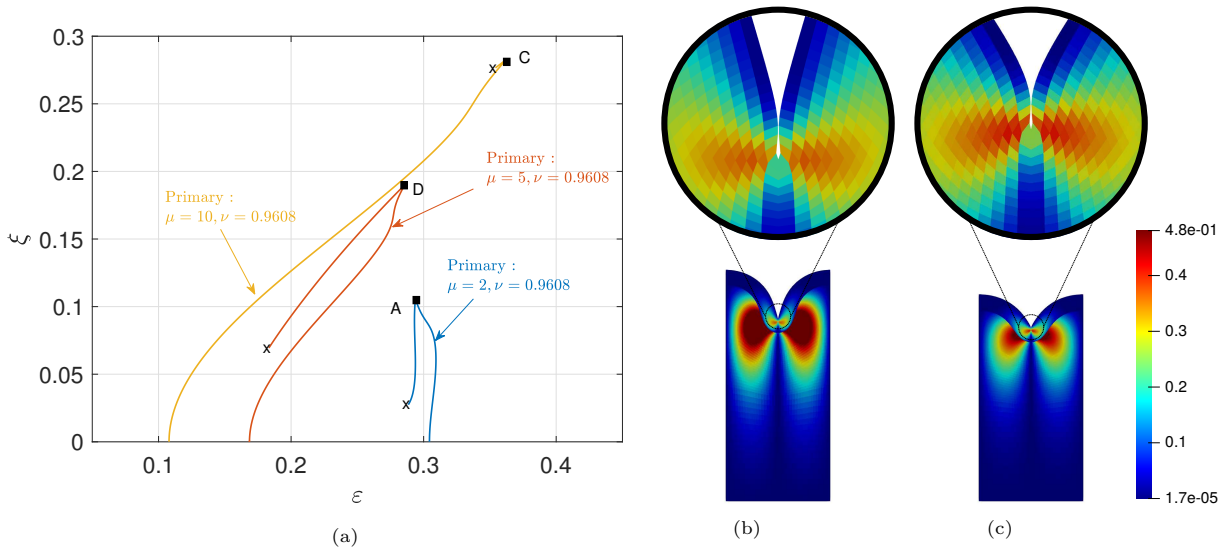

(a) (b) (c)

Figure 12: Influence of film-to-substrate stiffness ratio μ_f/μ_s on the evolution of the localized deformation pattern. In (a) primary bifurcation orbit, plotted in ε vs. ξ, for a nearly incompressible Neo-Hookean bilayer ($H_f/H = 0.1$, $\nu = 0.9608$) for three different values of the stiffness ratio: $\mu_f/\mu_s = 2$ (see also Figure 5b) and $\mu_f/\mu_s = 5,\ 10$. In (b) the localized deformation pattern (fold) for the $\mu_f/\mu_s = 10$ case plotted at point C. In (c) the localized deformation pattern (fold) for the $\mu_f/\mu_s = 5$ case plotted at point D. Deformed configurations also show contours for the absolute value of the Lagrangian strain shear component $|E_{12}|$.

We have thus established that the highly localized deformation solutions of creases and folds found in the literature, can be obtained using the path-following bifurcation technique used here, guided by group theory in view of the large symmetry group of the problem at hand, without the use of imperfections.

[28]The results in Figures 11 and 12 use solid lines for the bifurcated paths but this should not be interpreted to indicate stability information.

4.5. Equilibria of the Infinite Perfect Homogeneous Layer via Control Parameter Switching

Although our primary focus has been on layered and graded inhomogeneous elastic systems, understanding the solution set of the homogeneous problem is of equal importance in establishing the nature (local bifurcation or not) of creasing and folding solutions in free-surface instability mechanics problems. Researchers having only experience with relatively simple nonlinear buckling problems can easily underestimate the severe difficulties involved in finding bifurcated solutions to the homogeneous Biot problem. The Biot singularity occurs simultaneously at all wavelengths and this massive degeneracy effectively thwarts trial-and-error (including imperfection) methods for selecting an initial guess for use in Newton-Raphson based iterative solvers. In this subsection we employ the innovative *imperfection-free* systematic parameter-switching scheme of Healey and Miller (2007) to discover solutions to the homogeneous Biot problem.

Thus far the results presented in Figures 7 to 9 were obtained by using compressive strain ε as a control parameter while fixing the film-to-substrate shear modulus ratio ($\mu_f/\mu_s = 2$). We now proceed to discuss the evolution of deformation of the body as the continuation parameter is switched to μ_f/μ_s with ε fixed. By switching the control parameter to μ_f/μ_s for a fixed ε one can obtain bifurcated equilibrium orbits for the homogeneous halfspace ($\mu_f = \mu_s$) without the need to introduce an imperfection in a structure whose exponentially decaying bifurcation eigenmode (corresponding to Biot's surface instability) has a vanishingly small wavelength.

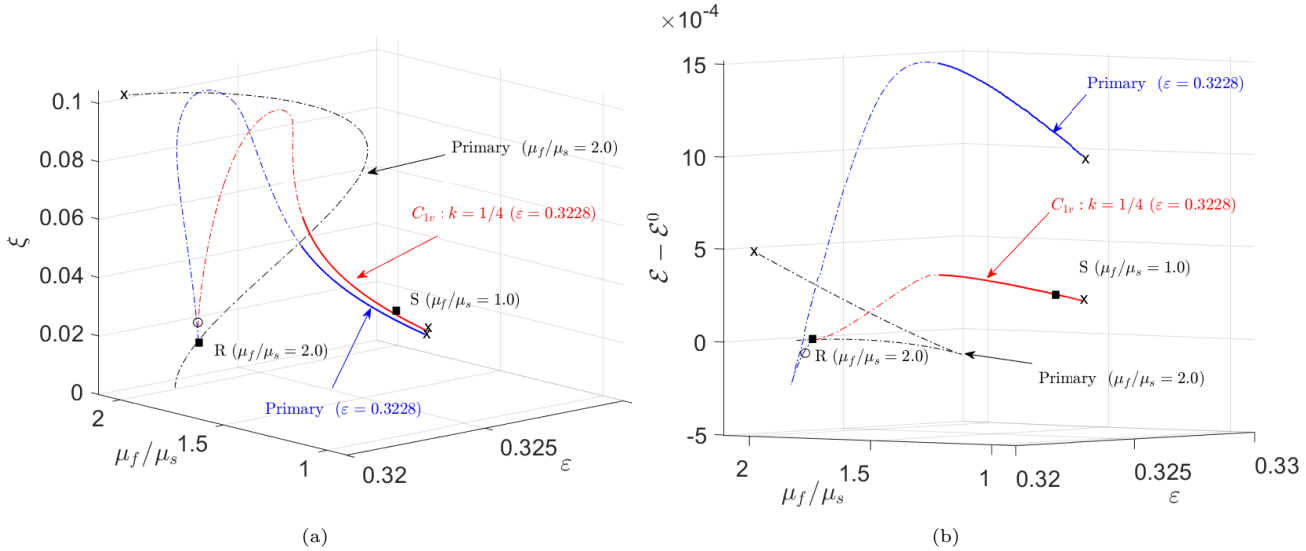

Figure 13: An efficient way to obtain creased, bifurcated solutions for the homogeneous halfspace problem by switching the control parameter of an equilibrium orbit from strain ε to shear moduli ratio μ_f/μ_s in a Neo-Hookean bi-layer. The axonometric projections show: (a) Amplitude ξ as a function of strain ε and moduli ratio μ_f/μ_s. (b) Energy change $(\mathcal{E} - \mathcal{E}^0)$ as a function of strain ε and shear moduli ratio μ_f/μ_s. Equilibrium solutions for the homogeneous Neo-Hookean halfspace are found for $\mu_f/\mu_s = 1$. Solid and dot-dashed lines correspond, respectively, to the stable and unstable parts of these equilibrium paths, based on Bloch-wave analysis of a $q = 4$, $(L_d = 4L_c)$ supercell.

We work with the bilayer structure and a domain of length $L_d = 4L_c$. Bifurcation diagrams for this case are shown in Figure 13. As before, we begin by loading a bi-layer of $\mu_f/\mu_s = 2$ with increasing strain ε on the principal path and locate the primary bifurcation point. The segment of the primary orbit for $\mu_f/\mu_s = 2.0$ and ε as the continuation parameter is plotted in black dashed line (unstable C_{4v} orbit, identical to the primary path in Figure 7). On this (primary bifurcation) orbit of the bi-layer with $\mu_f/\mu_s = 2$, we switch the continuation parameter from ε to μ_f/μ_s at point R as seen in Figure 13. The primary path where μ_f/μ_s is the control parameter evolves along the blue curve, corresponding to a C_{4v} orbit with a fixed $\varepsilon = 0.3228$. In the neighborhood of point R the C_{4v} orbit bifurcates into a lower symmetry C_{1v} orbit corresponding to $k = 1/4$, plotted in red dashed line (unstable). As seen in Figure 13a, the amplitude of deformation initially increases and subsequently decreases as $\mu_f/\mu_s \longrightarrow 1$ leading to a stable solution at $\mu_f/\mu_s = 1.0$,

i.e. for the homogeneous body. As expected, the deformed configuration at point S exhibits a localized surface deformation. For a fixed $\varepsilon = 0.3228$, at a given μ_f/μ_s the energy of the system on the C_{4v} orbit is higher than the corresponding one for its lower symmetry bifurcated counterpart C_{1v} as seen in Figure 13b. With this approach, we have found *without the need of introducing an imperfection*, a bifurcated equilibrium solution of the perfect homogeneous layer, whose lowest strain instability is a surface one with a vanishing wavelength, i.e. has a critical wavenumber $\omega_c \longrightarrow \infty$ (see Biot (1963)).

5. Conclusion

It is well-known that a linearized stability analysis of a compressed halfspace with a flat free surface predicts wrinkles (see Biot (1963)) and hence precludes a perfect halfspace model from *locally* bifurcating from the flat state to a creased/folded one. The nucleation of this localization phenomenon is a poorly understood (see Yang et al. (2021)) issue in hyperelastic solids. While the methods employed in the existing literature avoid this inconvenient fact by introducing an "*a priori*" imperfection (geometric or surface force) which biases the system toward the desired configuration, the choice of imperfection introduces an *uncontrolled perturbation to the exploration of the transition from the flat state to localized creases and/or folds*. It is exactly this transition issue which we have eliminated in this work. Using the imperfection-free local bifurcation and global solution branch following method introduced in Pandurangi et al. (2020), we employ a group-theoretic approach for perfect structures.

To demonstrate the methodology, we select a stable (polyconvex) material model and consider two plane-strain boundary value problems: *a functionally graded* layer whose shear modulus varies exponentially with distance from the free surface, and *a thin-film on a substrate* layer. Application of the imperfection-free local bifurcation and global solution branch following method shows that highly localized (creased) stable equilibrium solutions evolve "*far*" from the initial smooth and oscillatory bifurcation near the flat trivial solution. Furthermore, we find that isolated stable creases (i.e., a single crease surrounded by long flat regions) evolve, along the *long wavelength secondary bifurcating paths*, "*far*" from the flat trivial solution, as seen in the bifurcation diagrams of Figures 7, 8 and 9. These secondary paths bifurcate in a cascading fashion from the short wavelength, wrinkled, primary bifurcation paths. These primary paths in turn emerge from the system's symmetry-breaking bifurcation points along its flat configuration path. These qualitative results are robust to parameter variation in the material model ranging over strain-softening to Neo-Hookean to strain-hardening materials.

Taking the method one step further, we employ a multiparameter approach akin to that of Healey and Miller (2007); Healey and Sipos (2013); Healey et al. (2013), and switch continuation parameters in the bilayer problem. Here we use the film-to-substrate shear moduli ratio for continuation to obtain isolated crease solutions for the perfect homogeneous halfspace without using an imperfection, while avoiding analysis near the highly degenerate homogeneous state at the Biot instability.

With the present work we eliminate the uncontrolled effects of "*a-priori*" imperfections on the study of creasing and folding in compressed hyperelastic halfspaces and demonstrate that "*creases and folds are not local bifurcations*" as frequently reported in the literature.

ACKNOWLEDGMENTS

All authors would acknowledge support from the École Polytechnique and its Laboratore de Mécanique des Solides (LMS). The work was initiated in part by grants from École Polytechnique and the C.N.R.S. (Centre National de Recherche Scientifique) during the AY 2017-2018, while TJH was a Distinguished Visiting Professor and SSP a visiting doctoral student. RSE acknowledges several visits to LMS during this period supported by the LMS. The work of SSP was also supported in part by the National Science Foundation (NSF) through grant DMS-1613753. TJH also acknowledges partial support from that grant and from NSF grant DMS-2006586. The work of RSE was also partially supported by the NSF grant CMMI-1462826, and he acknowledges the Minnesota Supercomputing Institute (MSI) at the University of Minnesota for providing resources that contributed to the research results reported within this work. http://www.msi.umn.edu.

6. References

References

Aberg, M., Gudmundson, P., 1997. The usage of standard finite element codes for computation of dispersion relations in materials with periodic microstructure. The Journal of the Acoustical Society of America 102, 2007 – 2013.

Agmon, S., Douglis, A., Nirenberg, L., 1964. Estimates near the boundary for solutions of elliptic partial differential equations satisfying general boundary conditions ii. Communications on Pure and Applied Mathematics 17, 35–92.

Akerson, A., Elliott, R.S., 2021. Stability and post-bifurcation of film-substrate systems. Proceedings of the Royal Society of London A: Mathematical, Physical and Engineering Sciences Submitted.

Allgower, E.L., Georg, K., 2003. Introduction to Numerical Continuation Methods. volume 45 of *Classics In Applied Mathematics*. SIAM.

Alzetta, G., Arndt, D., Bangerth, W., Boddu, V., Brands, B., Davydov, D., Gassmoeller, R., Heister, T., Heltai, L., Kormann, K., Kronbichler, M., Maier, M., Pelteret, J.P., Turcksin, B., Wells, D., 2018. The `deal.II` library, version 9.0. Journal of Numerical Mathematics 26, 173–183.

Audoly, B., Arezki, B., 2008a. Buckling of a stiff film bound to a compliant substrate—part i, formulation, linear stability of cylindrical patterns, secondary bifurcations. Journal of the Mechanics and Physics of Solids 56.

Audoly, B., Arezki, B., 2008b. Buckling of a stiff film bound to a compliant substrate—part ii, a global scenario for the formation of herringbone pattern. Journal of the Mechanics and Physics of Solids 56, 2422 – 2443.

Audoly, B., Azreki, B., 2008. Buckling of a stiff film bound to a compliant substrate—part iii: Herringbone solutions at large buckling parameter. Journal of the Mechanics and Physics of Solids 56, 2444 – 2458.

Ball, J.M., 1976. Convexity conditions and existence theorems in nonlinear elasticity. Archive for Rational Mechanics and Analysis 63, 337 – 403.

Biot, M.A., 1963. Surface instability of rubber in compression. Applied Scientific Research, Section A 12, 168 – 182.

Cao, Y., Hutchinson, J.W., 2012. From wrinkles to creases in elastomers: the instability and imperfection-sensitivity of wrinkling. Proceedings of the Royal Society of London A: Mathematical, Physical and Engineering Sciences 468, 94 – 115.

Chen, D., Cai, S., Suo, Z., Hayward, R.C., 2012. Surface energy as a barrier to creasing of elastomer films: An elastic analogy to classical nucleation. Physical Review Letters 109, 038001.

Chen, D., Jin, L., Suo, Z., Hayward, R.C., 2014. Controlled formation and disappearance of creases. Materials Horizon 1, 207 – 213.

Chen, Y.C., Yang, S., L, W., 2018. Surface instability of elastic half-spaces by using the energy method. Proceedings of the Royal Society of London A: Mathematical, Physical and Engineering Sciences 474.

Chossat, P., Lauterbach, R., 2000. Methods in Equivariant Bifurcations and Dynamical Systems. volume 15 of *Advanced Series in Nonlinear Dynamics*. World Scientific.

Ciarletta, P., 2018. Matched asymptotic solution for crease nucleation in soft solids. Nature Communications 9, 1 – 7.

Diab, M., Kim, K.S., 2014. Ruga-formation instabilities of a graded stiffness boundary layer in a neo-hookean solid. Proceedings of the Royal Society of London A: Mathematical, Physical and Engineering Sciences 470.

Diab, M., Zhang, T., Zao, R., Gao, H., Kim, K.S., 2013. Ruga mechanics of creasing: from instantaneous to setback creases. Proceedings of the Royal Society A: Mathematical, Physical and Engineering Sciences A 469, 20120753.

Eskandari, M., Javili, A., Kuhl, E., 2016. Elastosis during airway wall remodeling explains multiple co-existing instability patterns. Journal of Theoretical Biology 403, 209 – 218.

Field, M., 1996. Lectures on bifurcations, dynamics and symmetry. Number 356 in Pitman Research Notes in Mathematics, Longman.

Gatermann, K., Hohmann, A., 1991. Symbolic exploitation of symmetry in numerical pathfollowing. IMPACT of Computing in Science and Engineering 3, 330 – 365.

Gent, A.N., Cho, I.S., 1999. Surface instabilities in compressed or bent rubber blocks. Rubber Chemistry and Technology 72, 253 – 262.

Golubitsky, M., Stewart, I., Schaeffer, D.G., 1988. Singularities and Groups in Bifurcation Theory. Volume 2. volume 69 of *Applied Mathematical Sciences*. First ed., Springer-Verlag.

Healey, T., Miller, U., 2007. Two-phase equilibria in the anti-plane shear of an elastic solid with interfacial effects via global bifurcation. Proceedings of the Royal Society A: Mathematical, Physical and Engineering Sciences 463, 1117 – 1134.

Healey, T., Sipos, A., 2013. Computational stability of phase-tip splitting in the presence of small interfacial energy in a simple two-phase solid. Physica D 261, 62 – 69.

Healey, T.J., 1988. A group-theoretic approach to computational bifurcation problems with symmetry. Computer Methods in Applied Mechanics and Engineering 67, 257 – 295.

Healey, T.J., 1989. Why bifurcation: A study of a reticulated dome, in: Ang, A.H.S. (Ed.), Structures Congress '89, Sessions related to design, analysis and testing - San Francisco, California, United States - May 1-5, 1989, pp. 942 – 948.

Healey, T.J., Li, Q., Cheng, R.B., 2013. Wrinkling behavior of highly stretched rectangular elastic films via parametric global bifurcation. Journal of Nonlinear Science 23, 777 – 805.

Hill, R., Hutchinson, J., 1975. Bifurcation phenomena in the plain strain tension test. Journal of the Mechanics and Physics of Solids 23, 239 – 264.

Hohlfeld, E., Mahadevan, L., 2011. Unfolding the sulcus. Physical Review Letters 106, 105702.

Hohlfeld, E., Mahadevan, L., 2012. Scale and nature of sulcification patterns. Physical Review Letters 109, 025701.

Hutchinson, J., 2013. The role of nonlinear substrate elasticity in the wrinkling of thin films. Proceedings of the Royal Society A: Mathematical, Physical and Engineering Sciences A 371.

Ikeda, K., Murota, K., 2010. Imperfect Bifurcation in Structures and Materials: Engineering Use of Group-Theoretic Bifurcation Theory. volume 149 of *Applied Mathematical Sciences*. Second ed., Springer.
Iooss, G., Joseph, D.D., 1990. Elementary Stability and Bifurcation Theory. Second ed., Springer.
Jin, L., Auguste, A., Hayward, R.C., Suo, Z., 2015. Bifurcation diagrams for the formation of wrinkles or creases in soft bilayers. Journal of Applied Mechanics 82, 061008.
Jin, L., Chen, D., Hayward, R.C., Suo, Z., 2014. Creases on the interface between two soft materials. Soft Matter 10, 303 – 311.
Keller, H.B., 1987. Numerical Methods in Bifurcation Problems. Tata Institute of Fundamental Research/Springer, Bombay/New York.
Kielhöfer, H., 2012. Bifurcation Theory: An Introduction with Applications to Partial Differential Equations. volume 156 of *Applied Mathematical Sciences*. Second ed., Springer.
Knowles, J.K., Sternberg, E., 1976. On the failure of ellipticity of the equations for finite elastostatic plane strain. Archive for Rational Mechanics and Analysis 63, 321 – 336.
Lee, D., Triantafyllidis, N., Barber, J., Thouless, M., 2008. Surface instability of an elastic half space with material properties varying with depth. Journal of the Mechanics and Physics of Solids 56, 858 – 868.
Li, B., Cao, Y.P., Feng, X.Q., Gao, H., 2012. Mechanics of morphological instabilities and surface wrinkling in soft materials: a review. Soft Matter 8, 5728 – 5745.
Marsden, J.E., Hughes, T.J.R., 1983. Mathematical Foundations of Elasticity. Prentice Hall.
McWeeny, R., 2002. Symmetry: An introduction to group theory and its applications. Courier Dover Publications.
Negrón-Marrero, P.V., Montes-Pizarro, E.L., 2011. The complementing condition and its role in a bifurcation theory applicable to nonlinear elasticity. New York Journal of Mathematics 17a, 245–265.
Pandurangi, S., Elliott, R., Healey, T., Triantafyllidis, N., 2020. Stable spatially localized configurations in a simple structure – a global symmetry-breaking approach. Journal of Elasticity 142, 163 – 199.
Rosakis, P., 1997. Characterization of convex isotropic functions. Journal of Elasticity 49, 257 – 267.
Sattinger, D.H., 1979. Group Theoretic Methods in Bifurcation Theory. volume 762 of *Lecture Notes in Mathematics*. Springer-Verlag.
Silling, S.A., 1991. Creasing singularities in compressible elastic materials. Journal of Applied Mechanics 58, 70 – 74.
Simpson, H.C., Spector, S.J., 1987. On the positivity of the second variation in finite elasticity. Arch. Rat. Mech. Anal. 98, 1–30.
Singh, M., Pipkin, A., 1965. Note on ericksen's problem. J. Appl. Math. Phys. (ZAMP) 16, 706 –709.
Triantafyllidis, N., 1980. Bifurcation phenomena in pure bending. Journal of the Mechanics and Physics of Solids 28, 221 – 245.
Triantafyllidis, N., Peek, R., 1992. On stability and the worst imperfection shape in solids with nearly simultaneous eigenmodes. International Journal of Solids and Structures 29, 2281 – 2299.
Truesdell, C., Noll, W., 1965. The Non-Linear Field Theories of Mechanics. volume 3 of *Encyclopedia of Physics*. Springer-Verlag.
Vanderbauwhede, A., 1982. Local Bifurcation and Symmetry. Research Notes in Mathematics, Pitman.
Wohlever, J.C., Healey, T.J., 1995. Group theoretic approach to the global bifurcation analysis of axially compressed cylindrical shell. Comput. Meth. Appl. Mech. Engr 122.
Yang, P., Fang, Y., Yuan, Y., Meng, S., Nan, Z., Xu, H., Imtiaz, H., Liu, B., Gao, H., 2021. A perturbation force based approach to creasing instability in soft materials under general loading conditions. Journal of the Mechanics and Physics of Solids 151, 104401–1 – 104401–10.
Zhao, R., Zhang, T., Diab, M., Gao, H., Kim, K.S., 2015a. The primary bilayer ruga-phase diagram i: Localizations in ruga evolution. Extreme Mechanics Letters 4, 76 – 82.
Zhao, Y., han, X., Li, G., Lu, C., Cao, Y., Feng, X.Q., Gao, H., 2015b. Effect of lateral dimension on the surface wrinkling of a thin film on compliant substrate induced by differential growth swelling. Journal of the Mechanics and Physics of Solids 83.
Zhao, Z., Diab, M., Kim, K.S., 2016. The primary bilayer ruga-phase diagram ii: Irreversibility in ruga evolution. Journal of Applied Mechanics .

Appendix A. Group-Theoretic Considerations

The fundamental concept used to study the bifurcated equilibrium paths and their stability in any conservative elastic system is the existence of a group G of transformations that leave its energy – e.g. $\mathcal{E}(\mathbf{u};\varepsilon)$ defined in (2.1) for the problem at hand – unchanged, i.e., invariant under the action of all transformations $g \in G$. More specifically, to each element $g \in G$ we associate a unitary transformation T_g (termed "*representation*" of g) acting on $\mathbf{u}(\mathbf{X}) \in U$ with image $T_g[\mathbf{u}] \in U$ that satisfies

$$\mathcal{E}(T_g[\mathbf{u}];\varepsilon) = \mathcal{E}(\mathbf{u};\varepsilon)\,; \quad \forall \varepsilon \geq 0\,,\ \forall \mathbf{u} \in U\,,\ \forall g \in G\,, \tag{A.1}$$

where ε is the scalar load parameter (assumed positive) and U the space of admissible functions $\mathbf{u}$.

It follows from (A.1) that the variation of $\mathcal{E}$ with respect to its argument $\mathbf{u}$ (first order functional derivative $\mathcal{E}_{,\mathbf{u}}$) possess the property of "*equivariance*"

$$(T_g[\mathcal{E}_{,\mathbf{u}}(\mathbf{u};\varepsilon)],\delta\mathbf{u}) = (\mathcal{E}_{,\mathbf{u}}(T_g[\mathbf{u}];\varepsilon),\delta\mathbf{u})\,; \quad \forall\varepsilon\geq 0\,,\ \forall\mathbf{u},\delta\mathbf{u}\in U\,,\ \forall g\in G\,. \tag{A.2}$$

According to (2.2), the system's equilibrium solutions $\mathbf{u}(\mathbf{X};\varepsilon)$ are found by extremizing its energy; consequently all solutions of the system $(\mathcal{E}_{,\mathbf{u}}(\mathbf{u};\varepsilon),\delta\mathbf{u})$ must satisfy (A.2). It is more appropriate to talk about "*orbits*" of equilibrium paths since, in view of the equivariance described in (A.2), applying to an equilibrium solution $\mathbf{u}$ the transformation T_g automatically generates another equilibrium solution $T_g[\mathbf{u}]$.

A subset of these equilibrium solutions, termed "*principal solutions*" and denoted by $\overset{0}{\mathbf{u}}(\mathbf{X};\varepsilon)$, are invariant under all transformations T_g. These solutions belong to an invariant subspace of U, denoted by $\mathcal{S}_G$ and called the "*fixed-point space*" of the group G

$$(\mathcal{E}_{,\mathbf{u}}(\overset{0}{\mathbf{u}}(\mathbf{X};\varepsilon);\varepsilon),\delta\mathbf{u}) = 0\,,\ \forall\varepsilon\geq 0\,; \quad \overset{0}{\mathbf{u}}\in\mathcal{S}_G := \{\mathbf{u}\in U \mid\ T_g[\mathbf{u}]=\mathbf{u}\,,\ \forall g\in G\}\,. \tag{A.3}$$

The benefit of finding the fixed point space of the group is that to determine the principal solution $\overset{0}{\mathbf{u}}(\mathbf{X};\varepsilon)$ one no longer needs to search in the full space U but only its subspace $\mathcal{S}_G\subset U$. This is a significant advantage, especially in numerical calculations, since the dimension of the fixed point space is considerably lower than the corresponding one of the full space.

To determine the stability of the principal solution, one has to check the positive definiteness of the self-adjoint bilinear operator $\mathcal{E}^0_{,\mathbf{uu}}$, evaluated on the principal path $\overset{0}{\mathbf{u}}(\mathbf{X};\varepsilon)$, by finding its eigenvalues $\beta(\varepsilon)$

$$((\mathcal{E}^0_{,\mathbf{uu}},\Delta\mathbf{u}),\delta\mathbf{u}) = \beta(\varepsilon)\langle\Delta\mathbf{u},\delta\mathbf{u}\rangle\,; \quad \forall\delta\mathbf{u}\in U\,;\ \mathcal{E}^0_{,\mathbf{uu}} := \mathcal{E}_{,\mathbf{uu}}(\overset{0}{\mathbf{u}}(\mathbf{X};\varepsilon);\varepsilon)\,, \tag{A.4}$$

where $\Delta\mathbf{u}$ is the corresponding eigenmode and $\langle\cdot\ ,\ \cdot\rangle$ denotes an inner product in U. A stable solution corresponds to a positive minimum eigenvalue[29] β and the Bloch-wave representation may be used, as described in Section 2.2. For a well-posed problem, its stress-free (unloaded) configuration at $\varepsilon=0$ is stable; as the load increases stability will be lost at the first bifurcation point encountered along the loading path at some ε_c.

It can be shown, e.g. see Golubitsky et al. (1988); McWeeny (2002), that the existence of the group G implies the existence of a symmetry basis with respect to which (i) the operator $\mathcal{E}^0_{,\mathbf{uu}}$ defined in (A.4) can be block-diagonalized and (ii) the space of admissible functions $U=\oplus_{\mu=1}^{h}V^\mu$ can be uniquely decomposed into a direct sum of mutually orthogonal invariant subspaces V^μ (with h being the number of equivalence, or conjugacy, classes for G). Each subspace V^μ is associated with an n_μ-dimensional irreducible representation τ^μ of G, also termed "*irrep*" from which an appropriate projection operator can be constructed giving the V^μ component of any function in U. With each irrep τ^μ, we can associate its "*kernel*" $G^\mu\subseteq G$ where $G^\mu=\{g\in G\mid\tau^\mu_g=I\}$, with I the n_μ-dimensional identity matrix.

Bifurcated equilibrium paths, termed "*primary*", can emerge from the principal path at a generic *μ-type* symmetry-breaking bifurcation point corresponding to irrep τ^μ at load ε_c having n_μ zero eigenvalues of $\mathcal{E}^c_{,\mathbf{uu}}$. That is, $\beta(\varepsilon_c)=0$ so that

$$((\mathcal{E}^c_{,\mathbf{uu}},\overset{i}{\mathbf{u}}),\delta\mathbf{u}) = 0\,,\ \overset{i}{\mathbf{u}}\in\mathcal{N}_\mu\,,\ \langle\overset{i}{\mathbf{u}},\overset{j}{\mathbf{u}}\rangle=\delta_{ij}\,,\ i,j=1,\ldots,n_\mu\,;\ \forall\delta\mathbf{u}\in U\,;\ \mathcal{E}^c_{,\mathbf{uu}} := \mathcal{E}_{,\mathbf{uu}}(\overset{0}{\mathbf{u}}(\mathbf{X};\varepsilon_c);\varepsilon_c)\,, \tag{A.5}$$

where the eigenmodes $\overset{i}{\mathbf{u}}$ span the n_μ-dimensional null space $\mathcal{N}_\mu\subseteq V^\mu$. Moreover, these eigenmodes are invariant under all transformations belonging to G^μ. Some additional conditions, termed "*transversality conditions*" must also hold to ensure that ε_c is a bifurcation and not a limit point:

$$\det\left[((\left[d\mathcal{E}^0_{,\mathbf{uu}}/d\varepsilon\right]_c,\overset{i}{\mathbf{u}}),\overset{j}{\mathbf{u}})\right]\neq 0\,. \tag{A.6}$$

[29] See Footnote 10.

The (primary) bifurcated orbits $\overset{b}{\mathbf{u}}(\mathbf{X};\varepsilon)$ emerging from $\overset{0}{\mathbf{u}}(\mathbf{X};\varepsilon)$ at ε_c, can be computed efficiently by using their own *isotropy subgroup* $H \supseteq G^\mu$, i.e., the elements of the subgroup of G satisfying $T_g[\overset{b}{\mathbf{u}}] = \overset{b}{\mathbf{u}}$, thus finding the bifurcated orbits in the corresponding fixed-point space[30] $\mathcal{S}_\mathcal{H}$. Along this path there may occur (secondary) bifurcation points. In such cases, the above procedure begins once again with $\overset{b}{\mathbf{u}}(\mathbf{X};\varepsilon)$ as the new principal path from which — secondary with respect to $\overset{0}{\mathbf{u}}(\mathbf{X};\varepsilon)$ — bifurcated orbits will emerge.

Group theory also allows us to determine if the corresponding bifurcation point is "*transverse*" (asymmetric) or "*pitchfork*" (symmetric). To this end once has to first find the normalizer $N_G(H)$ of the isotropy subgroup H, defined by $N_G(H) = \{g \in G \mid gHg^{-1} = H\}$. A bifurcation is transverse if $N_G(H) = H$ and pitchfork if $H \subset N_G(H)$.

To reiterate, the strategy followed in this work is to sequentially apply the above-described procedure to follow the bifurcating equilibrium orbits of the system by identifying, each time, their symmetry group and their corresponding fixed-point space. As we proceed from the principal solution to the primary bifurcations emerging from it, then to the secondary bifurcations emerging from the primary ones, the corresponding symmetry groups and fixed-point spaces change accordingly. Knowledge of the symmetries of a path allows for an efficient calculation of a unique solution in its own fixed-point space. The method adopted here follows the procedures introduced by Healey (1988); Gatermann and Hohmann (1991). Moreover, following Gatermann and Hohmann (1991); Chossat and Lauterbach (2000); Pandurangi et al. (2020), knowledge of the lattice of isotropy subgroups of the initial symmetry group guides the search for the bifurcated equilibrium paths in a systematic way and explains our findings.

Appendix A.1. Principal Solution, Irreps, and Bifurcations – Group $G = C_{\infty v}$

As described in Subsection. 2.4, the fixed-point space of $C_{\infty v}$ for the layered system consists of only the trivial principal solution $\overset{0}{\mathbf{u}}(\mathbf{X};\varepsilon) = \mathbf{0}$. According to group theory (e.g., Ikeda and Murota (2010)) $C_{\infty v}$ has two 1-dimensional irreps (one being the trivial identity irrep). These provide the possibility of simple bifurcations to paths with symmetry groups of C_∞. There are also an infinity of 2-dimensional irreps, providing the possibility of double bifurcations. These correspond to bifurcating paths with symmetry groups C_{nv}, where $n \in \mathbb{N}$, as shown in Table A.1.

n_μ	Irrep μ	$\tau^\mu_{c(\phi)}$	$\tau^\mu_{\sigma_v}$	G^μ	Bifurc. Orbit Sym.
1	A	1	1	$C_{\infty v}$	No Bif.
1	B	1	-1	C_∞	C_∞
2	E_n	$\begin{bmatrix} \cos(n\phi) & -\sin(n\phi) \\ \sin(n\phi) & \cos(n\phi) \end{bmatrix}$ $n = 1, 2, 3 \cdots$	$\begin{bmatrix} 1 & 0 \\ 0 & -1 \end{bmatrix}$	C_n	C_{nv}

Table A.1: Table of irreps and bifurcated orbit symmetries for $G = C_{\infty v}$. The first column gives the dimension n_μ of the corresponding irrep; the second column gives a standard label/name for the irrep; the third and fourth columns provide the corresponding irrep matrix for the generators $\tau^\mu_{c(\phi)}$ and $\tau^\mu_{\sigma_v}$, respectively; the fifth column gives the *kernel of* τ^μ (i.e., $G^\mu = \{g \in G \mid \tau^\mu_g = I\}$, where I is the n_μ-dimensional identity matrix.); the sixth column gives the symmetry group of the corresponding bifurcating equilibrium path(s).

The possibility of C_{nv} bifurcated equilibrium orbits for the $C_{\infty v}$ group, corresponding to the two-dimensional E_n irreps, comes from the fact that the system has an energy and thus its stability operator $\mathcal{E}_{,\mathbf{uu}}$ is self-adjoint.

[30] Principal as well as primary bifurcated solutions belong to $\mathcal{S}_H$; each bifurcated orbit can be found separately by using the *equivariant branching lemma* (see Vanderbauwhede (1982)).

Appendix A.2. Primary Bifurcation Orbit at ε_c, Irreps, and Bifurcations – Group $G = C_{qv}$

In Section 4.1 we find only double bifurcations at each ε (since each ε can be interpreted as the ε_{min} of (4.3)) with corresponding eigenmodes $\cos(2\pi X_1/L_c)\delta\mathbf{u}^c(X_2)$ and $\sin(2\pi X_1/L_c)\delta\mathbf{u}^s(X_2)$ — as expected from the 2-dimensional irreps of $C_{\infty v}$ of Table A.1. No simple bifurcations are found, in spite of the existence of 1-dimensional irreps of this group. From the infinity of primary bifurcation paths that can be constructed at each ε, we follow next the bifurcation orbit emerging from the lowest load ε_c. Every linear combination of the two eigenmodes is left invariant by the elements of the group C_q, the critical point corresponds to the $\mu = E_q$ irrep, and according to the general theory (see Table A.1) the symmetry group of the bifurcating orbit is C_{qv}. This symmetry group is finite and has the following two generators: $c(2\pi/q)$ and σ_v. Recall also that $q \in \mathbb{N}$ is determined by the size of the domain $\Omega_d = [-L_d/2, L_d/2] \times [0, H]$ considered ($L_d = qL_c$). Calculations for the primary bifurcation orbit of symmetry C_{qv} are done in the corresponding fixed point space $S_{C_{qv}}$ using the domain $[0, L_c/2] \times [0, H]$ by imposing $u_1(0, X_2) = 0$ in addition to the remaining admissibility conditions for the displacement field.

As indicated in Table A.2, this group has four 1-dimensional irreps (one being the trivial identity irrep). For even values of q lower symmetry ($C_{(q/2)v}$) simple bifurcation orbits are possible. There are also $\lfloor (q-1)/2 \rfloor$ 2-dimensional irreps, providing the possibility of double bifurcations where the correspond to bifurcating orbits have smaller symmetry groups C_{rv}, where $r := \gcd(j, q)$, with $j = 1, \ldots, \lfloor (q-1)/2 \rfloor$.

n_μ	Irrep μ	$\tau^\mu_{c(2\pi/q)}$	$\tau^\mu_{\sigma_v}$	G^μ	Bifurc. Orbit(s) Sym.
1	A_1	1	1	C_{qv}	No Bif.
1	A_2	1	-1	C_q	C_q
1	B_1	- 1	1	$C_{(q/2)v}$	$C_{(q/2)v}$
1 (q: even)	B_2	- 1	-1	$C_{(q/2)v}$	$C_{(q/2)v}$
2	E_j	$\begin{bmatrix} \cos(2\pi j/q) & -\sin(2\pi j/q) \\ \sin(2\pi j/q) & \cos(2\pi j/q) \end{bmatrix}$ $1 \le j \le \lfloor (q-1)/2 \rfloor$	$\begin{bmatrix} 1 & 0 \\ 0 & -1 \end{bmatrix}$	C_r $r := \gcd(j, q)$	C_{rv}

Table A.2: Table of irreps and bifurcated orbit symmetries for $G = C_{qv}$. The first column gives the dimension n_μ of the corresponding irrep; the second column gives a standard label/name for the irrep; the third and fourth columns provide the corresponding irrep matrix for the generators $\tau^\mu_{c(2\pi/q)}$ and $\tau^\mu_{\sigma_v}$, respectively; the fifth column gives the *kernel of* τ^μ (i.e., $G^\mu = \{g \in G \mid \tau^\mu_g = I\}$, where I is the n_μ-dimensional identity matrix.); the sixth column gives the symmetry group of the corresponding bifurcating equilibrium path(s). The function $\gcd(a, b)$ is the greatest common divisor of a and b, while the notation $\lfloor a \rfloor$ denotes the lowest integer closest to a.

Appendix A.3. Secondary Bifurcation Orbits and their Symmetry

In this work, to avoid lengthy numerical calculations we choose $q = 4$. From Table A.1 the primary bifurcation orbit has C_{4v} symmetry. Consequently, from Table A.2 and recalling the general form of the eigenmode at (2.5), the secondary bifurcation orbit of the two-dimensional irrep $j = 1$ corresponds to $k = 1/4$ (and $k = 3/4$ by symmetry) has C_{1v} symmetry and is unique, although it emerges from a double bifurcation point.[31] The secondary bifurcated orbit of the one-dimensional irrep corresponds to $k = 1/2$ and has C_{2v} symmetry and is again unique since it corresponds to a simple bifurcation. To decide the nature of these orbits – transverse or pitchfork – we must find the normalizers of their symmetry groups, C_{1v} and C_{2v}. For the double bifurcation points: $N_{C_{4v}}(C_{1v}) = C_{2v} \supset C_{1v}$ and for the simple bifurcation point: $N_{C_{4v}}(C_{2v}) = C_{4v} \supset C_{2v}$. Consequently, according to the general theory discussed at the first part of Appendix A, all secondary orbits have a global pitchfork type bifurcation.

[31] The two eigenmodes of this point are symmetry related and hence all bifurcated paths belong to the same orbit.

Appendix B. Material (Local) Stability and Principal Solution Analytical Calculations

To avoid distraction in the main body of this paper, a number of important calculations are presented here; proof of the polyconvexity for the constitutive law of Subsection 2.3 in Appendix B.1, components of the first Piola-Kirchhoff stress and tangent moduli of the principal solution in Appendix B.2.

Appendix B.1. Local Stability of the Constitutive Law

The energy density function $W(\mathbf{F};X_2)$ cannot be strictly convex with respect to $\mathbf{F}$ as it violates the property of material frame indifference and would imply the existence of a unique minimizer of $\mathcal{E}(\mathbf{u})$ in (2.1), thus precluding the expected non-uniqueness of equilibrium solutions due to buckling phenomena. Although global stability is impossible due to buckling, local stability in the sense of Hadamard (see Truesdell and Noll (1965)) makes sense since even for finite strains most elastomeric materials do not exhibit solutions with strain discontinuity. In mathematical terms this property requires "*rank one convexity*" of $W(\mathbf{F};X_2)$ i.e. convexity only with respect to rank one deformation gradient tensors $\mathbf{F}=\mathbf{a}\otimes\mathbf{n}$, where $\mathbf{a},\mathbf{n}$ are arbitrary unit vectors.

Showing that a particular constitutive law is rank one convex, even in the simplest case of an isotropic material in 2D, is an algebraically tedious exercise that is often impossible to prove analytically (see Knowles and Sternberg (1976)). Fortunately, the stronger restriction of "*polyconvexity*" introduced by Ball (1976) is easier to verify and sufficient to ensure the sought rank one convexity. In this section, we first show that the material models (2.6) and (2.8) satisfy the conditions of polyconvexity for $p>0.5$.

To prove polyconvexity for an isotropic hyperelastic material in plane strain, one has to express its stain energy $W(\mathbf{F})$ (homogeneous material considered here with no loss of generality) as a function of $\lambda_1,\lambda_2,\delta$, where λ_1,λ_2, are the principal stretch ratios of $\mathbf{F}$ and $\delta\equiv\lambda_1\lambda_2$, and show convexity of this function with respect to its three arguments considered as independent. To this end the energy density (2.8) is written as

$$
\begin{aligned}
&W(\mathbf{F})=\psi(\lambda_1,\lambda_2,\delta)\equiv\mu\left[\frac{c}{2}[f(\lambda_1,\lambda_2)+2g(\delta)]^p+\frac{\nu}{1-\nu}(\delta-1)^2\right]\,,\\
&f(\lambda_1,\lambda_2)\equiv(\lambda_1-\lambda_2)^2\geq 0\,;\quad g(\delta)\equiv\delta-1-\ln\delta\geq 0\,,
\end{aligned}
\tag{B.1}
$$

where the functions f and g are minimized respectively at $\lambda_1=\lambda_2$ and $\delta=1$ making $\psi=0$ the global minimum at these values.

Following Rosakis (1997), the necessary and sufficient conditions for polyconvexity of $W(\mathbf{F})$ in (B.1) requires the following three conditions to ensure the convexity of the symmetric in λ_1,λ_2 function $\psi(\lambda_1,\lambda_2,\delta)$

$$
\begin{aligned}
&A)\quad \psi(\lambda_1,\lambda_2,\delta)=\psi(\lambda_2,\lambda_1,\delta)\,,\\
&B)\quad \psi(\lambda_1+\beta,\lambda_2+\beta,\delta)\geq\psi(\lambda_1,\lambda_2,\delta),\ \forall\beta\geq 0\,,\\
&C)\quad \mathbf{H}=\begin{bmatrix}\dfrac{\partial^2\psi}{\partial\lambda_1\partial\lambda_1} & \dfrac{\partial^2\psi}{\partial\lambda_1\partial\lambda_2} & \dfrac{\partial^2\psi}{\partial\lambda_1\partial\delta}\\ & \dfrac{\partial^2\psi}{\partial\lambda_2\partial\lambda_2} & \dfrac{\partial^2\psi}{\partial\lambda_2\partial\delta}\\ \text{Sym.} & & \dfrac{\partial^2\psi}{\partial\delta^2}\end{bmatrix}=\begin{bmatrix}\mathcal{K} & -\mathcal{K} & \mathcal{L}\\ \text{Sym.} & \mathcal{K} & -\mathcal{L}\\ & & \mathcal{M}\end{bmatrix}\quad\text{be positive semidefinite}\,,
\end{aligned}
\tag{B.2}
$$

$$
\mathcal{K}\equiv\mu cp(f+2g)^{(p-2)}((2p-1)f+2g)\,,\quad \mathcal{L}\equiv 2\mu cp(p-1)(f+2g)^{(p-2)}\sqrt{f}\left(\frac{\delta-1}{\delta}\right)\,,
$$

$$
\mathcal{M}\equiv\mu\left[cp\frac{(f+2g)^{(p-2)}}{\delta^2}\left((2p-2)(\delta-1)^2+(f+2g)\right)+\frac{2\nu}{1-\nu}\right].
$$

As $\det \mathbf{H} = 0$, positive semi-definiteness relies on the non-negativity of the nontrivial first ($\mathcal{K} \geq 0,\ \mathcal{M} \geq 0$) and second ($\mathcal{K}\mathcal{M} - \mathcal{L}^2$) ≥ 0 order principal minors of $\mathbf{H}$, which can be shown to hold for $p \geq 0.5$ and $1 > \nu > 0.05$, thus establishing the sought polyconvexity and hence rank one convexity of the power-law constitutive model.

Appendix B.2. First Piola-Kirchhoff Stress and Incremental Moduli Tensors

The nonzero components of the first Piola-Kirchhoff stress $\overset{0}{S}_{ij}$ and the incremental moduli $\overset{0}{L}_{ijkl}$, based on the energy in (2.8) and evaluated on the principal solution $\overset{0}{\mathbf{F}} = \mathrm{diag}[\lambda_1, \lambda_2]$ are given by

$$
\begin{aligned}
\overset{0}{S}_{11}/\mu &= \exp(\alpha X_2)\left[\eta(\lambda_1 - \frac{1}{\lambda_1}) + \frac{2\nu}{1-\nu}(\lambda_1\lambda_2 - 1)\lambda_2\right] , \\
\overset{0}{S}_{22}/\mu &= \exp(\alpha X_2)\left[\eta(\lambda_2 - \frac{1}{\lambda_2}) + \frac{2\nu}{1-\nu}(\lambda_1\lambda_2 - 1)\lambda_1\right] ,
\end{aligned}
$$

$$
\begin{aligned}
\overset{0}{L}_{1111}/\mu &= \exp(\alpha X_2)\left[\zeta\left(\frac{\lambda_1^2-1}{\lambda_1}\right)^2 + \eta\left(\frac{\lambda_1^2+1}{\lambda_1^2}\right) + \frac{2\nu}{1-\nu}\lambda_2^2\right] , \\
\overset{0}{L}_{2222}/\mu &= \exp(\alpha X_2)\left[\zeta\left(\frac{\lambda_2^2-1}{\lambda_2}\right)^2 + \eta\left(\frac{\lambda_2^2+1}{\lambda_2^2}\right) + \frac{2\nu}{1-\nu}\lambda_1^2\right] , \\
\overset{0}{L}_{1212}/\mu &= \overset{0}{L}_{2121}/\mu = \eta\exp(\alpha X_2) , \\
\overset{0}{L}_{2112}/\mu &= \overset{0}{L}_{1221}/\mu = \exp(\alpha X_2)\left[\eta\left(\frac{1}{\lambda_1\lambda_2}\right) + \frac{2\nu}{1-\nu}(1-\lambda_1\lambda_2)\right] , \\
\overset{0}{L}_{1122}/\mu &= \overset{0}{L}_{2211}/\mu = \exp(\alpha X_2)\left[\zeta\left(\frac{\lambda_1^2-1}{\lambda_1}\right)\left(\frac{\lambda_2^2-1}{\lambda_2}\right) + \frac{2\nu}{1-\nu}(2\lambda_1\lambda_2 - 1)\right] .
\end{aligned}
\tag{B.3}
$$

$$
\zeta = 2p(p-1)c(\lambda_1^2 + \lambda_2^2 - 2 - 2\ln\lambda_1\lambda_2)^{p-2}, \quad \eta = pc(\lambda_1^2 + \lambda_2^2 - 2 - 2\ln\lambda_1\lambda_2)^{p-1}.
$$

Note that for the Neo-Hookean material, i.e when $p = 1$, we have $\zeta = 0, \eta = 1$. For the graded material $\alpha > 0$, $\mu = \mu_0$ while for the bilayer $\alpha = 0$ with $\mu = \mu_f$ for the film and $\mu = \mu_s$ for the substrate.

Appendix C. Mesh-dependence of Numerical Calculations

The localized deformation patterns of creases and folds that appear in Figures 11 and 12 are mesh-sensitive. This is because the creasing/folding behavior observed is related to the Biot halfspace instability whose eigenmodes span all wavelengths. Consequently, equilibrium paths are sensitive to the underlying numerical discretization.

To explore the effects of mesh dependence, we study a Neo-Hookean bi-layer with layer thickness $H_f/H = 0.1$, $\mu_f/\mu_s = 2$ and $\nu = 0.8182$ using progressively refined meshes of (i) 4, (ii) 8 and (iii) 12 elements through the film thickness. The discretized domain considered is $\Omega_d = [-L_d/2, L_d/2] \times [0, H]$ ($q = 1$) with periodic end conditions, as to capture the primary bifurcation orbit and the corresponding secondary bifurcation points. The primary bifurcation orbits are plotted in Figure C.1 with (i) 550 elements and 4,400 degrees of freedom (blue curve), (ii) 2,200 elements and 17,600 degrees of freedom (red curve), and (iii) 4,950 elements and 39,600 degrees of freedom (yellow curve). Local mesh refinement is used near the point $(0, H)$ where localization develops. The bifurcation point corresponding to the first secondary orbit is also calculated and denoted by an open circle. Also note that stability results were not calculated for the finer meshes, thus the solid lines used in Figure C.1 do not contain stability information.

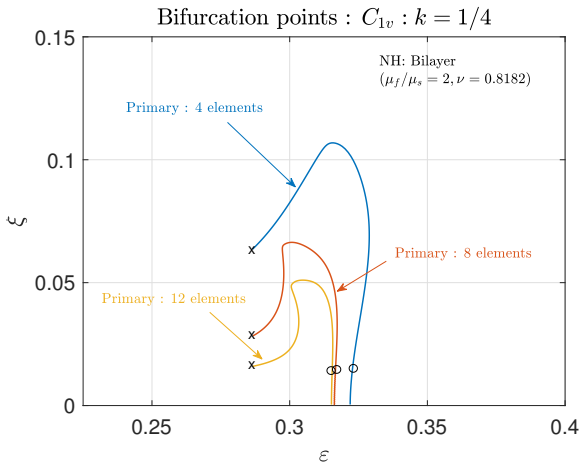

Figure C.1: Influence of mesh refinement for a Neo-Hookean bilayer with layer thickness $H_f/H = 0.1$, $\mu_f/\mu_s = 2$ and $\nu = 0.8182$ showing the ε vs. ξ the primary bifurcation orbit for progressively refined meshes using 4, 8 and 12 elements through the thickness of the film. The bifurcation amplitude corresponding to the onset of the first secondary orbit (marked by an open circle) is insensitive to mesh refinement.

The initial part of the primary bifurcation orbit is rather insensitive to the mesh used (results are practically indistinguishable up to $\xi \approx 0.05$ for the two finer meshes) as is the bifurcation point of the secondary orbit C_{1v}. As the deformation localizes, it is expected that the orbits will become more mesh-dependent although their overall shape remains very similar: a maximum amplitude ξ is reached, followed by a drastic snap-back under decreasing applied strain ε. Mesh dependence is also expected for the secondary orbits, see Figure 7b, although the meshing effects on these paths were not systematically explored. The results here indicate that our main results, presented in Section 4, are accurate and independent of the mesh in a sizable neighborhood surrounding the initial primary bifurcation point including the period-extending secondary bifurcations and emerging paths. However, as all bifurcating paths evolve away from this neighborhood the results become mesh dependent.